

Unique Word-Based Frame Design for Bistatic Integrated Sensing and Communication

Roberto Bomfin and Marwa Chafii, *Senior Member, IEEE*

Abstract—Integrated sensing and communication (ISAC) aims at enhancing the network functionalities and enabling new applications in the upcoming communications networks. In this paper, we propose two unique word (UW)-based frame designs for bistatic ISAC. The approach consists of replacing the cyclic prefix (CP) with a Zadoff-Chu (ZC)-based sequence. With this approach, the radar receiver does not need to know the data symbols to perform sensing and the data rate is not compromised by the addition of extra pilots. The sensing performance of the UW-based frames is compared with that of orthogonal frequency division multiplexing (OFDM) as well as the pilot-symbol (PS) based radar processing. We derive the Cramér-Rao bound (CRB) considering a band-limited system with raised-cosine filtering. Furthermore, we provide low-complexity fast Fourier transform (FFT)-based radar receivers that perform integer and fine grid multi-target delay-Doppler (DD) estimations. For the integer FFT-based receiver, an upper bound for the outlier probability is derived when the true DD falls outside the integer grid. The results demonstrate that the UW frames exhibit competitive radar performance with PS while having a 16.67% higher data rate for the cases investigated.

Index Terms—ISAC, bistatic sensing, unique word, delay-Doppler, OFDM

I. INTRODUCTION

THE recent advancements in wireless communications and radar technologies have been taking similar paths by employing antenna array techniques and moving toward higher frequency bands, leading to similarities in hardware architecture, channel characteristics, and signal processing. This trend yields a unique opportunity for the integrated sensing and communication (ISAC) into the same network infrastructure, which has been considered as a new technology for future networks by academia and industry [1]–[4]. Many applications that take advantage of ISAC have been considered, including smart factoring, the Internet of Things, robotics, environmental monitoring, and vehicular communications.

One of the major challenges of ISAC is the design of unified waveforms, whose objective is to use the same signal to perform both communication and sensing tasks. In this regard, three categories have been conceived, namely, sensing-centric design (SCD), communication-centric design (CCD), and joint design (JD). In short, the SCD approach incorporates communication on top of an existing sensing technology [5], [6]. Conversely, the CCD’s goal is to include sensing in a communications-only system [7]–[10]. Lastly, the JD’s idea is to develop new waveforms along with beamforming

techniques [11]–[13]. Each strategy has its pros and cons, and their adoption is dependent on the particular application and ISAC scenario. Additionally, there are many possibilities for the sensing architecture in ISAC, namely, uplink and downlink signaling, monostatic, bistatic, and multistatic sensing configurations. The choice of each configuration depends on the application, and multiple combinations of different configurations are possible. For instance, the downlink-monostatic ISAC represents a typical ISAC scenario where the base station senses objects within its adjacency, which can be improved by uplink-bistatic sensing as demonstrated in [14].

In this work, we propose a novel frame design for bistatic downlink ISAC where both communications and sensing aspects are simultaneously considered, which can be considered as a type of joint design. When the ISAC operates within a communication network, the typical solution is to perform sensing tasks using communication waveforms, such as orthogonal frequency division multiplexing (OFDM), orthogonal time frequency space (OTFS), and others. In [7], [8], the authors show the feasibility of performing radar processing using OFDM signals. More recently, many works have considered OTFS due to its delay-Doppler (DD) domain processing [15]–[17]. While radar processing using these waveforms works well in monostatic sensing, it is more challenging in the bistatic setting because it can be infeasible for the radar to know the transmitted data.

Given the practical difficulties in performing sensing using the data blocks, a typical approach to realize sensing using the communication infrastructure is to make use of the known signals within the frame to perform sensing. In the context of the IEEE 802.11 standard, this can be done using the preamble composed of the short training field and the channel estimation field (CEF). In [18], the authors show how to perform sensing for the IEEE 802.11ad frame using the preamble in a monostatic mmWave sensing. More recently, the authors in [19] have demonstrated a practical bistatic sensing setup exploiting the Golay sequences used for channel estimation in IEEE 802.11ay. In the 5th generation (5G) of communications systems, a similar approach can be taken by using the positioning reference signal (PRS). The PRSs are time-frequency resources within the resource block structure of 5G that enables parameter estimation. An approach of using PRS to perform sensing is shown in [20] as a pilot signal in ISAC.

When the pilot-based ISAC is designed specifically for sensing as in the PRS case, or when CEF is made more frequent in the IEEE 802.11 frame to improve sensing, the available data rate for communication is decreased. Motivated by this problem, in this work we propose to include a deterministic

Roberto Bomfin is with the Engineering Division, New York University (NYU) Abu Dhabi, 129188, UAE (email: roberto.bomfin@nyu.edu).

Marwa Chafii is with Engineering Division, New York University (NYU) Abu Dhabi, 129188, UAE and NYU WIRELESS, NYU Tandon School of Engineering, Brooklyn, 11201, NY, USA (email: marwa.chafii@nyu.edu).

signal in the guard interval instead of the cyclic prefix (CP), such that the sensing signal does not compete with the data resources. This approach is known in the literature to aid channel estimation [21]–[24], and is termed as a unique word (UW) scheme. In [21], the authors introduce the idea of replacing the CP with the UW to improve the synchronization for single-carrier (SC) systems. In [22], the authors show how to track the time-varying channel using the UWs for SC, while the work [23] focuses on phase-tracking. In [24], we have shown that the UW-based frame design achieves higher spectral efficiency than the CP-based systems for multiple-input multiple-output (MIMO) generalized frequency division multiplexing (GFDM) and OFDM. Moreover, when the CP is removed or replaced by the UW, the CP-restoration technique [25], [26] can be utilized to reconstruct the CP at the receiver. That is, although removing or replacing the CP breaks the circular convolution structure of the channel, the frequency-domain equalization remains very similar to the CP transmission.

In this paper, we combine the DD processing techniques for parameter estimation with the UW-based frame design and propose a new frame for ISAC, which is partially presented in [27]. The UW-based frame is advantageous for two reasons, namely, it does not require the radar receiver to know the communication data, and it does not incur data rate loss for communication. Specifically, we design two UW signals based on the well-known Zadoff-Chu (ZC) sequence. The first scheme has the same size as the CP and is termed UW1. To enable a relatively simple fast Fourier transform (FFT)-based DD estimation, we use the CP-restoration technique [26], which leads to a loss in signal-to-noise ratio (SNR). To avoid the SNR loss, a second scheme consisting of two ZC sequences with half the size of the CP is considered, which is termed UW2. The drawback of this second frame is that the estimation range is reduced. However, we show that there can be cases where this reduction is not prohibitive, e.g., in the indoor environment. Another advantage of these sequences is to enhance LoS synchronization similar to the approach of [19], where the slow time-varying time-offset (TO) and carrier frequency offset (CFO) between the transmitter and radar nodes can be compensated. There are several methods for TO and CFO cancellation available in the literature as shown by [28]. In this work, we address the TO and CFO compensation by an offset cancellation method in the delay-Doppler domain, since the TO and CFO are common to the LoS and target paths. Both UW1 and UW2 frames are compared to the OFDM and pilot-symbol (PS) benchmarks. Here we note that OFDM has been chosen because it performs better than OTFS due to lower waterfall SNR, as shown in [15]. For simplicity, we consider a PS approach that replaces a whole OFDM symbol as a pilot. Additionally, we highlight that we consider a model with limited bandwidth based on the root-raised cosine (RRC) filter as [18], which is typically not considered in other works in the literature. In terms of theoretical results, we provide the Cramér-Rao bound (CRB) that is valid for all frames, namely, UW1, UW2, OFDM, and PS. The FFT-based multi-target estimator with LoS interference removal is derived and evaluated. Another useful theoretical result is the derivation of the outlier probability upper bound (UB) in regards to the

integer DD grid. Differently from [15], our analysis considers the case where the true DD falls outside the grid search, yielding a novel expression. Lastly, we provide a comparative range analysis of the investigated frames. The results reveal that both UW frames are competitive against the PS approach. In particular, the UW1 frame is more suitable in outdoor deployment where the unambiguous range is broader. In indoor deployments where the unambiguous range is not critical, the UW2 is more suitable, since it achieves the CRB.

In summary, the contributions are as follows

- Proposal of two UW-based frames for ISAC that do not require the knowledge of the data by the radar unit, and do not incur data rate reduction for communication.
- Derivation of the band-limited model with RRC filtering and its corresponding CRB.
- Derivation of fine grid FFT-based multi-target DD estimator with LoS interference removal with TO and CFO cancellation.
- Derivation of the outlier probability UB for the integer grid FFT-based estimator. Two approximations for the UB are presented due to the numerical intractability of the exact solution.
- Range comparison between the UW frames with the benchmarking frames, OFDM, and PS. The results show competitive performance in favor of UW.

The remainder of the paper is organized as follows. In Section II, the general system model and frames schemes are presented. In Section III, the discrete-time channel model is shown with a suitable approximation that enables the FFT-based processing. In Section IV, the CRB and DD estimators are derived. In Section V, the outlier probability expression and its approximations are presented. In Section VI, a frame design comparison is provided with all frames. The numerical results are shown in Section VII. Finally, Section VIII concludes the paper.

Notation: Vectors and matrices are denoted by lowercase and uppercase bold symbols as \mathbf{x} and \mathbf{X} , respectively, with indexing $\mathbf{x}[n]$ and $\mathbf{X}[n, m]$ returning the n th element of the vector, and the element in the n th row and m th column of the matrix. The modulo operation is denoted as $(a)_N$. The transpose, conjugated transpose and conjugate are denoted by $(\cdot)^T$, $(\cdot)^H$ and $(\cdot)^\dagger$, respectively. $\mathbf{A} \odot \mathbf{B}$ and $\mathbf{A} \oslash \mathbf{B}$ are the element-wise product and division between two equal-sized matrices. The operations $(\mathbf{a} * \mathbf{b})[n]$ and $(\mathbf{a} \circledast \mathbf{b})[n]$ return the n th element of a linear and circular convolution between the vectors \mathbf{a} and \mathbf{b} , which should be equal-sized in the latter case. The normalized Fourier transform matrix of size N is \mathbf{F}_N where $\mathbf{F}_N \mathbf{F}_N^H = \mathbf{I}_N$. The expectation and variance operator are $\mathbb{E}(\cdot)$ and $\mathbb{V}(\cdot)$, respectively. The real part of a complex number a is $\mathcal{R}(a)$. For a real number a , $\text{round}(a) \in \mathbb{Z}$ returns the nearest integer to a . A real random variable x uniformly distributed between $[a, b]$ is denoted as $x \sim \mathcal{U}(a, b)$.

II. SYSTEM MODEL

In this work, we consider a bistatic radar system operating within a wireless network that serves communication users in the downlink. It is assumed that there is a line-of-sight (LoS)

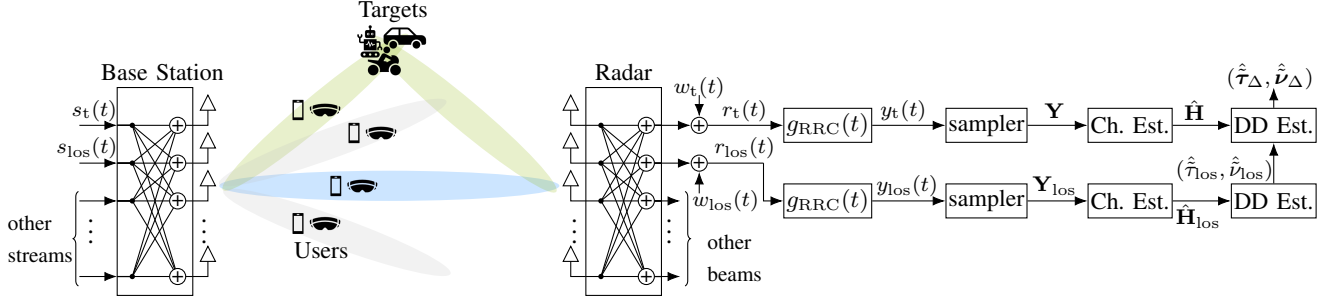


Fig. 1. Bistatic radar system model using communications signals. The received signals y_t and $y_{\text{los}}(t)$ are described in Section II. The sampled signals \mathbf{Y} and \mathbf{Y}_{los} are given in Section III. The channel estimates $\hat{\mathbf{H}}$ and $\hat{\mathbf{H}}_{\text{los}}$, and DD estimators are described in Section IV.

beam between the base station (BS) and radar, such that the target's parameter estimation is performed in relation to the LoS component. An illustration of the system is shown in Fig. 1. In the following, four different signaling schemes are considered. The benchmarking schemes are OFDM and PS, while the proposed frames are UW1 and UW2.

A. Transmit Signals with Different Frames

In this work, we focus on the delay-Doppler processing, hence the spatial parameters such as angle-of-arrival and angle-of-departure are abstracted in the model for simplicity¹. The transmit signal of an arbitrary spatial stream is composed of the concatenation of M sub-blocks of $K + N_{\text{cp}}$ samples each as

$$\mathbf{x} = [\tilde{\mathbf{x}}_0^T \ \tilde{\mathbf{x}}_1^T \ \cdots \ \tilde{\mathbf{x}}_{M-1}^T]^T, \quad (1)$$

where $\tilde{\mathbf{x}}_m \in \mathbb{C}^{K+N_{\text{cp}}}$ is the m th sub-block and $\mathbf{x} \in \mathbb{C}^{N_x}$ is the concatenation of all sub-blocks and $N_x = M(K + N_{\text{cp}})$. The quantities K and N_{cp} are the FFT and CP sizes, respectively. Once the discrete-time signal is generated, the continuous-time signal is generated by filtering using the RRC filter $g_{\text{RRC}}(t)$ as

$$s(t) = \sum_{n=0}^{N_x-1} \mathbf{x}[n]g_{\text{RRC}}(t - nT_s), \quad (2)$$

where T_s is the sampling interval, which is related to the bandwidth as $B = 1/T_s$. In this work, we consider two spatial streams, namely, one associated with the LoS whose signals are termed $s_{\text{los}}(t)$ and \mathbf{x}_{los} , and ones associated with the targets are termed $s_t(t)$ and \mathbf{x}_t . We highlight that this notation has been chosen to derive the model with respect to the radar receiver and in practice $s_{\text{los}}(t)$ and $s_t(t)$ are seen as two arbitrary spatial streams from the base station viewpoint.

In the following, we show how $\tilde{\mathbf{x}}_m$ is generated by each transmission scheme considered in this manuscript. A diagram is depicted in Fig. 2.

1) *OFDM*: the m th OFDM signal is

$$\mathbf{x}_m = \mathbf{F}_K^H \mathbf{d}_m, \quad (3)$$

¹In general the BS does not know the targets' positions. Thus, the beam which coincidentally hits a set of targets is processed by the radar, as illustrated by Fig. 1.

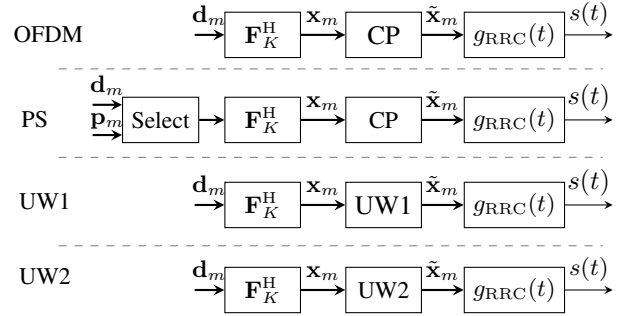


Fig. 2. Block diagram of frame schemes of an arbitrary spatial stream.

where \mathbf{d}_m is a quadrature amplitude modulation (QAM) symbol vector of size K with $\mathbb{E}(\mathbf{d}_m \mathbf{d}_m^H) = \mathbf{I}_K$ for all m . The CP is added according to

$$\tilde{\mathbf{x}}_m[n] = \mathbf{x}_m[(n - N_{\text{cp}})K], \quad (4)$$

for $n = 0, 1, \dots, K + N_{\text{cp}} - 1$ such that $\tilde{\mathbf{x}}_m \in \mathbb{C}^{K+N_{\text{cp}}}$ has the first N_{cp} samples composed by the CP.

2) *PS*: In this case, the sub-blocks with indexes belonging to $\mathcal{M}_p = \{0, M/M_p, 2M/M_p, \dots, (M_p - 1)M/M_p\}$ with $M_p = |\mathcal{M}_p|$ elements are the PS $\mathbf{p}_m \in \{-1, 1\}^K$, which is essentially a pilot signal with the same size as the data symbol. The m th sub-block is given by

$$\mathbf{x}_m = \begin{cases} \mathbf{F}_K^H \mathbf{p}_m, & m \in \mathcal{M}_p \\ \mathbf{F}_K^H \mathbf{d}_m, & m \in \mathcal{M}_d \end{cases}, \quad (5)$$

where the data set \mathcal{M}_d is disjoint to \mathcal{M}_p such that $\mathcal{M}_p \cup \mathcal{M}_d = \{0, 1, \dots, M - 1\}$. The CP is added similarly to (4).

3) *UW1*: The UW1 frame has the OFDM waveform in all sub-blocks according to (3), but instead of CP, the deterministic signal $\mathbf{x}_{\text{uw}} \in \mathbb{C}^{N_{\text{cp}}}$ is appended. The UW1 is by the N_{cp} size ZC sequence as

$$\mathbf{x}_{\text{uw1}}[n] = \exp(-j\pi n^2/N_{\text{cp}}), \quad (6)$$

for $0 \leq n < N_{\text{cp}}$. Then the m th sub-block $\tilde{\mathbf{x}}_m \in \mathbb{C}^{K+N_{\text{cp}}}$ with UW1 transmission is given by

$$\tilde{\mathbf{x}}_m = [\mathbf{x}_{\text{uw1}}^T \ \mathbf{x}_m^T]^T. \quad (7)$$

4) *UW2*: The UW2 transmission has a similar concept to the UW1. The difference is that the UW2 signal $\mathbf{x}_{\text{uw2}} \in \mathbb{C}^{N_{\text{cp}}/2}$ is half the size of the ZC signal (6) as

$$\mathbf{x}_{\text{uw2}}[n] = \exp(-j\pi n^2/(N_{\text{cp}}/2)), \quad (8)$$

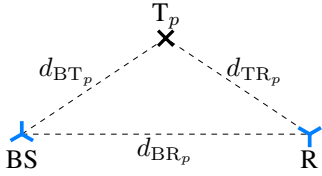


Fig. 3. Bistatic radar geometry.

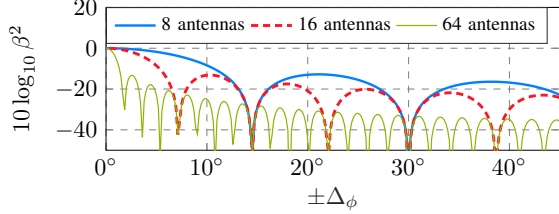


Fig. 4. Example of normalized ULA beam pattern that determines the LoS rejection for a given angle difference between the LoS and target beam.

for $0 \leq n < N_{cp}/2$, so that it needs to be appended twice before the OFDM symbol. Then the m th sub-block $\tilde{\mathbf{x}}_m \in \mathbb{C}^{K+N_{cp}}$ with UW2 transmission is given by

$$\tilde{\mathbf{x}}_m = [\mathbf{x}_{uw2}^T \quad \mathbf{x}_{uw2}^T \quad \mathbf{x}_m^T]^T. \quad (9)$$

The idea of using a ZC sequence with half the size in (8) is to allow a simpler radar receiver and to not incur interference as the one in (6). As it will be shown in Section VI, the UW2 signaling has half of the maximum unambiguous delay when the FFT-based radar receiver is used. Nevertheless, we note that it is possible to design a more sophisticated radar receiver that expands the maximum delay, which is not explored in this work.

B. Bistatic Radar Channel

In this work, we consider a scenario with P targets. An exemplary radar geometry is given in Fig. 3 for an arbitrary target with index $p \in \{0, 1, \dots, P-1\}$, where the distances in meters between the BS and target, target and radar, and BS and radar are denoted as d_{BT_p} , d_{TR_p} and d_{BR_p} , respectively. The time delay associated with each path is given by $\tau_{BT_p} = d_{BT_p}/c$, $\tau_{TR_p} = d_{TR_p}/c$ and $\tau_{BR_p} = d_{BR_p}/c$, where c is the speed of light. We consider the TO and CFO due to the asynchronicity between the BS and the radar to be unchanged during the coherent processing interval (CPI), which are denoted by τ_{to} and ν_{cfo} , respectively.

Based on the considerations above, the delay and frequency shift associated to the LoS are given by $\tau_{los} = \tau_{BT} + \tau_{to}$ and $\nu_{los} = \nu_{cfo}$, respectively. The delay and frequency shift for the path associated to the p th target are $\tau_p = \tau_{BT_p} + \tau_{TR_p} + \tau_{to}$ and $\nu_p = f_p + \nu_{cfo}$, where f_p is the frequency-shift due to Doppler.

Thus, the channel impulse response associated to the LoS path is $h_{los}(t, \tau) = h_{los}\delta(\tau - \tau_{los})e^{-j2\pi\nu_{los}t}$ with the channel gain h_{los} . And the radar channel impulse response for the p th target is $h_p(t, \tau) = h_p\delta(\tau - \tau_p)e^{-j2\pi\nu_p t}$ with the channel gain h_p . In practice, the channel gains $|h_p|^2$ and $|h_{los}|^2$ are determined by the well-known radar double-path and path-loss formulas, as considered in the high-level analysis of Subsection VII-C. The phase $\angle h_p$ and $\angle h_{los}$ are assumed to be unchanged during the CPI but random with a uniform distribution between 0 and 2π for each new frame and independent from one another.

We note that ultimately we are interested in estimating the difference $\tau_p - \tau_{los}$ and $\nu_p - \nu_{los}$ to infer the position of the target, where the TO and CFO effects are compensated since they are common for the LoS and target paths. This method can be categorized as one type of offset cancellation method in the delay-Doppler domain [28].

C. Received Signals

1) *Paths Associated to Targets:* Assuming that the radar channel stays constant during the transmission of $s_t(t)$, the received signal associated with the radar path after beamforming is given by

$$r_t(t) = \sum_{p=0}^{P-1} h_p s_t(t - \tau_p) e^{-j2\pi\nu_p t} + \beta h_{los} s_{los}(t - \tau_{los}) e^{-j2\pi\nu_{los} t} + w_t(t), \quad (10)$$

where $\beta \in [0, 1]$ represents the LoS rejection due to beamforming. For example, if the radar employs an ULA with 64 antennas, $\beta^2 = 1/100$ corresponding to a 20 dB of rejection is obtained if the LoS and the target are more than 5 degrees apart, i.e., $|\Delta\phi| > 5^\circ$ in Fig. 4. Lastly, $w_t(t)$ is the additive white Gaussian noise (AWGN). The model of (10) assumes that each target has one significant reflection to the radar.

The received signal is filtered using the same root-raised cosine filter as the transmitter

$$y_t(t) = \int r_t(t') g_{RRC}(t - t') dt'. \quad (11)$$

An approximation is given in equation (13) at the bottom of this page which is used in the simulation to simplify the model. This approximation is typically considered in the literature and assumes that the bandwidth of $g_{RRC}(t)$ is much larger than the maximum frequency shift. Intuitively, this means that the linear phase shift imposed by the channel is negligible within the time duration of the filter $g_{RRC}(t)$. In (11), $g_{RC}(t)$ is the raised cosine filter

$$g_{RC}(t) = \begin{cases} \frac{\pi}{4T_s} \text{sinc}\left(\frac{1}{2\alpha}\right), & t = \pm T_s/(2\alpha) \\ \frac{1}{T_s} \text{sinc}\left(\frac{1}{T_s}\right) \frac{\cos(\pi\alpha t/T_s)}{1 - (2\alpha t/T_s)^2}, & \text{otherwise} \end{cases} \quad (12)$$

$$y_t(t) \approx \sum_{p=0}^{P-1} h_p e^{-j2\pi\nu_p t} \sum_{n=0}^{N_x-1} \mathbf{x}_t[n] g_{RC}(t - nT_s - \tau_p) + \beta \left(h_{los} e^{-j2\pi\nu_{los} t} \sum_{n=0}^{N_x-1} \mathbf{x}_{los}[n] g_{RC}(t - nT_s - \tau_{los}) \right) + w'_t(t). \quad (13)$$

$$y_{los}(t) \approx h_{los} e^{-j2\pi\nu_{los} t} \sum_{n=0}^{N_x-1} \mathbf{x}_{los}[n] g_{RC}(t - nT_s - \tau_{los}) + \beta \left(\sum_{p=0}^{P-1} h_p e^{-j2\pi\nu_p t} \sum_{n=0}^{N_x-1} \mathbf{x}_t[n] g_{RC}(t - nT_s - \tau_p) \right) + w'_{los}(t) \quad (14)$$

with roll-off factor α .

2) *Path Associated to the LoS*: Analogously to (13), assuming that the radar channel stays constant during the transmission of $s_{\text{los}}(t)$, the approximate received signal associated with the LoS path is given in equation (14) at the bottom of the previous page.

III. DISCRETE-TIME RECEIVED SIGNAL

In the following, we describe how the passive radar samples $y_t(t)$ in (13) for each transmit signal of Subsection II-A. Additionally, a simplified model is derived, which is then used to design the DD estimator in Section IV. Although this section focuses on the targets branch of Fig. 1, the sampled signal associated with the LoS branch can be obtained by sampling $y_{\text{los}}(t)$ in (14) and following an analogous procedure.

A. OFDM Frame

In this case, the passive radar uses all OFDM sub-blocks to perform parameter estimation. As shown in the Appendix A, the received signal sampled at the sampling interval T_s is approximated as

$$\begin{aligned} \mathbf{Y}_{\text{ofdm}}[k, m] &= y_t(I_{\text{ofdm}}(k, m)T_s) \\ &\approx \sum_{p=0}^{P-1} h'_p \mathbf{u}_{M, \tilde{\nu}_p}[m] (\mathbf{x}_{t_m} \otimes \mathbf{g}_{K, \tilde{\tau}_p})[k] \\ &+ \beta h'_{\text{los}} \mathbf{u}_{M, \tilde{\nu}_{\text{los}}}[m] (\mathbf{x}_{\text{los}_m} \otimes \mathbf{g}_{K, \tilde{\tau}_{\text{los}}})[k] + \mathbf{W}_{\text{ofdm}}[k, m], \end{aligned} \quad (15)$$

where $I_{\text{ofdm}}(k, m)$ is the index mapper, $\mathbf{g}_{K, \tilde{\tau}_p}[k] = \tilde{g}_{\text{RC}}(k - \tilde{\tau}_p)$ is the discrete-time raised cosine filter for $k = 0, 1, \dots, K - 1$ and $\tilde{g}_{\text{RC}}(t) = g_{\text{RC}}(t_p/T_s)$, $\tilde{\tau}_p = \tau_p/T_s$ is the delay normalized to the sampling interval, which is in the interval $0 \leq \tilde{\tau}_p < N_{\text{cp}}$. We consider that the normalized LoS delay $\tilde{\tau}_{\text{los}} = \tau_{\text{los}}/T_s$ is in the interval $0 \leq \tilde{\tau}_{\text{los}} < 1$, i.e., the integer delay of the LoS path is in the first sample of the channel impulse response, which assumes that the system is synchronized with respect to the LoS. The frequency shift related component is $\mathbf{u}_{M, \tilde{\nu}_p}[m] = \exp(-j2\pi\tilde{\nu}_p m/M)$, where $\tilde{\nu}_p = \nu_p T_s N_x$ is the frequency shift normalized to subcarrier spacing of the whole signal if the bandwidth is divided by N_x . The noise term $\mathbf{W}_{\text{ofdm}}[k, m]$ has power σ_w^2 and is uncorrelated for different k and/or m .

Lastly, we note that for the OFDM frame, the spatial streams associated with the target and LoS have different OFDM symbols, which are distinguished in (15) by \mathbf{x}_{t_m} and $\mathbf{x}_{\text{los}_m}$, respectively.

B. PS Frame

When the passive radar performs the processing only based on the PS signals, the sampled signal is $\mathbf{Y}_{\text{ps}} \in \mathbb{C}^{K \times M_p}$ defined as

$$\begin{aligned} \mathbf{Y}_{\text{ps}}[k, m] &\approx \sum_{p=0}^{P-1} h'_p \mathbf{u}_{M_p, \tilde{\nu}_p}[m] (\mathbf{x}_m \otimes \mathbf{g}_{K, \tilde{\tau}_p})[k] \\ &+ \beta h'_{\text{los}} \mathbf{u}_{M_p, \tilde{\nu}_{\text{los}}}[m] (\mathbf{x}_m \otimes \mathbf{g}_{K, \tilde{\tau}_{\text{los}}})[k] + \mathbf{W}_{\text{ps}}[k, mM/M_p], \end{aligned} \quad (16)$$

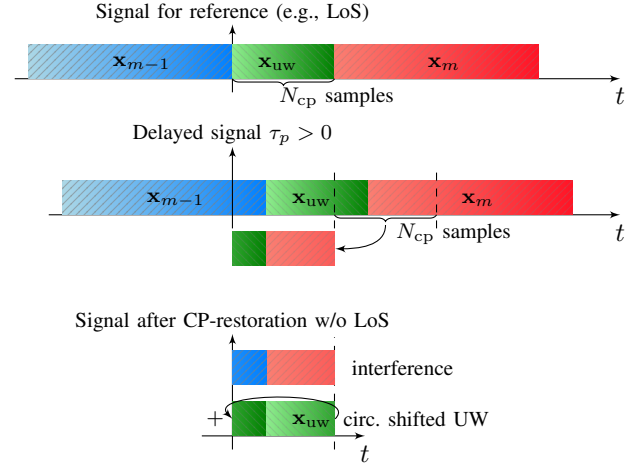


Fig. 5. Illustration of CP-restoration.

for $0 \leq k < K$ and $0 \leq m < M_p$, which has an analogous structure to \mathbf{Y}_{ofdm} in (15) by following the same steps, but with columns that respect $m \in \mathcal{M}_p$. Also, the noise sample of \mathbf{W}_{ps} have the noise power of \mathbf{W}_{ofdm} , σ_w^2 . It is important to notice that $\mathbf{u}_{M_p, \tilde{\nu}_l}$ has the same form as the one in (15) but with M_p instead of M . Another important distinction to (15) is that the pilot symbols are assumed to be the same for all spatial streams, which leads to the same signal \mathbf{x}_m for the target and LoS paths $\forall m \in \mathcal{M}_p$.

C. UW1 Frame with CP-restoration

For the UW1 transmission scheme, a frequency domain processing can be accomplished by the radar after performing the CP-restoration process similar to [25]. This process is illustrated in Fig. 5, which consists of adding the signals N_{cp} samples apart. The received signal is described in equation (24) at the bottom of the next page for $0 \leq k < N_{\text{cp}}$ and $0 \leq m < M$ such that $\mathbf{Y}_{\text{uw1}} \in \mathbb{C}^{N_{\text{cp}} \times M}$. The index mapper function $I_{\text{uw1}}(k, m) = (k + m(N_{\text{cp}} + K))$ ensures that the UW1 portion of the signal is sampled. Neglecting the AWGN noise, Fig. 5 demonstrates that the resulting signal is the cyclic convolved UW1 plus interference from the $(m-1)$ th and m th OFDM signals. Naturally, extra noise samples are also copied, so the resulting noise plus interference term is given in (25) at the bottom of the next page and has power

$$\begin{aligned} \mathbb{E}(\mathbf{W}_{\text{uw1}}[k, m] \mathbf{W}_{\text{uw1}}[k, m]^H) &\approx \\ 2\sigma_w^2 + \sum_{p=0}^{P-1} |h_p|^2 + \beta^2 |h_{\text{los}}|^2 &= \sigma_w^2 L_{\text{uw1}}. \end{aligned} \quad (17)$$

The AWGN power is counted twice due to the CP-restoration AWGN component in (25). The remaining terms are the interference from the $(m-1)$ th and m th OFDM signals. It is important to notice that for a given time index k , either the $(m-1)$ th or m th block has dominant power. This fact is depicted in Fig. 5 where the interference from the $(m-1)$ th and m th OFDM interference symbols are not superposed but

occupy different time slots. Thus, the power $|h_p|^2$ is added once and not twice. We can conveniently define

$$L_{\text{uw1}} = 2 + 1/\sigma_w^2 \left(\sum_{p=0}^{P-1} |h_p|^2 + \beta^2 |h_{\text{los}}|^2 \right) \quad (18)$$

as the SNR loss due to the additional interference terms. The approximations of (24) and (25) are due to the same reasons as the steps of (15).

D. UW2 Frame

In the case of the UW2 transmission, the radar samples the received signal as

$$\begin{aligned} \mathbf{Y}_{\text{uw2}}[k, m] &\approx \sum_{p=0}^{P-1} h'_p \mathbf{u}_{M, \tilde{\nu}_p}[m] (\mathbf{x}_{\text{uw2}} \otimes \mathbf{g}_{N_{\text{cp}}/2, \tilde{\tau}_p})[k] \\ &+ \beta h'_{\text{los}} \mathbf{u}_{M, \tilde{\nu}_{\text{los}}}[m] (\mathbf{x}_{\text{uw2}} \otimes \mathbf{g}_{N_{\text{cp}}/2, \tilde{\tau}_{\text{los}}})[k] + \mathbf{W}_{\text{uw2}}[k, m] \end{aligned} \quad (19)$$

for $0 \leq k < N_{\text{cp}}/2$ and $0 \leq m < M$ such that $\mathbf{Y}_{\text{uw2}} \in \mathbb{C}^{N_{\text{cp}}/2 \times M}$. \mathbf{Y}_{uw2} has an analogous structure to \mathbf{Y}_{ofdm} in (15) by following the same steps. Also, the noise sample of \mathbf{W}_{uw2} have the noise power of \mathbf{W}_{ofdm} , σ_w^2 . Differently from the other schemes, for the UW2 signal, it is assumed that the normalized delay is within the interval $0 \leq \tilde{\tau}_p < N_{\text{cp}}/2$, which decreases the maximum delay in which the radar can detect targets. Lastly, we note that the approximation in the second line of (19) is due to the same reasons as the steps of (15).

IV. TARGETS DELAY-DOPPLER (DD) ESTIMATION

This section starts with formulation of the DD MLE and CRB as benchmark. Then, to avoid the expensive computation of the MLE, we study a more practical solution for the multi-target DD estimation with LoS interference removal with reduced complexity that has two steps. First, the 2D channel is estimated in the DD domain with FFT processing for both target and LoS branches of the receiver depicted in Fig. 1. Subsequently, the *Fine Grid* algorithm is presented that removes inter-target and LoS interference.

A. Maximum Likelihood Estimator (MLE)

Assuming perfect LoS removal by setting $\beta = 0$, the MLE estimates DD pairs and channel gains of all reflections by minimizing the log-likelihood function

$$\hat{\Theta} = \min_{\Theta} \sum_{k, m} |\mathbf{Y}[k, m] - \mathcal{Y}_{\Theta}[k, m]|^2, \quad (20)$$

where $\mathbf{Y}[k, m]$ can be OFDM, PS, UW1 or UW2 as described in Section III and $\mathcal{Y}_{\Theta}[k, m]$ is the sampled noiseless received signal (13) without LoS interference

$$\begin{aligned} \mathcal{Y}_{\Theta}[k, m] &= \\ &\sum_{p=0}^{P-1} |h_p| e^{j\angle h_p} e^{-j2\pi \tilde{\nu}_p \frac{I(k, m)}{M(N_{\text{cp}} + K)}} \sum_{n=0}^{N_x-1} \mathbf{x}[n] \tilde{g}_{\text{RC}}(I(k, m) - n - \tilde{\tau}_p), \end{aligned} \quad (21)$$

with the true parameters $\Theta = [\theta_0^T \theta_1^T \dots \theta_{P-1}^T]^T \in \mathcal{R}^{4P \times 1}$ that is the concatenation of the parameters per target $\theta_p = [\tilde{\tau}_p \ \tilde{\nu}_p \ |h_p| \ \angle h_p]^T$. Also, we note that the sampling indexes $I(k, m)$ in (21) should be set accordingly for OFDM, PS, UW1 or UW2.

B. Cramér-Rao Bound (CRB)

The CRB for the likelihood function defined in the argument of the ML estimator in (20) is given in the following. The $4P \times 4P$ Fisher information matrix is given by

$$[\mathbf{I}(\Theta)]_{i, j} = \frac{2}{\sigma_w^2} \sum_{m, k} \mathcal{R} \left(\frac{\partial}{\partial \Theta_i} \mathcal{Y}_{\Theta}[m, k] \left(\frac{\partial}{\partial \Theta_j} \mathcal{Y}_{\Theta}[m, k] \right)^\dagger \right). \quad (22)$$

The partial derivative concerning the delay τ_p of the p th target is given by

$$\begin{aligned} \frac{\partial \mathcal{Y}_{\Theta}[m, k]}{\partial \tilde{\tau}_p} &= \\ &- |h_p| e^{j\angle h_p} e^{-j2\pi \tilde{\nu}_p \frac{I(k, m)}{N_x}} \sum_{n=0}^{N_x-1} \mathbf{x}[n] \tilde{g}'_{\text{RC}}(I(k, m) - n - \tilde{\tau}_p) \\ &+ \sum_{\substack{q=0 \\ q \neq p}}^{P-1} |h_q| e^{j\angle h_q} e^{-j2\pi \tilde{\nu}_q \frac{I(k, m)}{M(N_{\text{cp}} + K)}} \sum_{n=0}^{N_x-1} \mathbf{x}[n] \tilde{g}_{\text{RC}}(I(k, m) - n - \tilde{\tau}_q), \end{aligned} \quad (23)$$

$$\begin{aligned} \mathbf{Y}_{\text{uw1}}[k, m] &= y_t(I_{\text{uw1}}(k, m)T_s) + \underbrace{y_t((I_{\text{uw1}}(k, m) + N_{\text{cp}})T_s)}_{\text{CP-restoration}} \\ &\approx \sum_{p=0}^{P-1} h'_p \mathbf{u}_{M, \tilde{\nu}_p}[m] (\mathbf{x}_{\text{uw1}} \otimes \mathbf{g}_{N_{\text{cp}}, \tilde{\tau}_p})[k] + \beta h'_{\text{los}} \mathbf{u}_{M, \tilde{\nu}_{\text{los}}}[m] (\mathbf{x}_{\text{uw1}} \otimes \mathbf{g}_{K, \tilde{\tau}_{\text{los}}})[k] + \mathbf{W}_{\text{uw1}}[k, m] \end{aligned} \quad (24)$$

$$\begin{aligned} \mathbf{W}_{\text{uw1}}[k, m] &\approx \underbrace{w'_t(I_{\text{uw1}}(k, m)T_s)}_{\text{CP-restoration AWGN}} + \underbrace{w'_t((I_{\text{uw1}}(k, m) + N_{\text{cp}})T_s)}_{\text{LoS interference from } m\text{th block}} + \beta h'_{\text{los}} \mathbf{u}_{M, \tilde{\nu}_{\text{los}}}[m] (\mathbf{x}_m * \mathbf{g}_{K, \tilde{\tau}_{\text{los}}})[k] \\ &+ \sum_{p=0}^{P-1} \underbrace{h'_p \mathbf{u}_{M, \tilde{\nu}_p}[m-1] (\mathbf{x}_{m-1} * \mathbf{g}_{K, \tilde{\tau}_p})[k+K]}_{\text{interference from } (m-1)\text{th block}} + \underbrace{h'_p \mathbf{u}_{M, \tilde{\nu}_p}[m] (\mathbf{x}_m * \mathbf{g}_{K, \tilde{\tau}_p})[k]}_{\text{interference from } m\text{th block}} \end{aligned} \quad (25)$$

where the derivative of the raised cosine filter is shown in (33) at the bottom of the next page, whose details are omitted due to lack of space and have been validated using the Wolfram Mathematica software. The values for $t = 0$ and $\pm 1/(2\alpha)$ are defined by taking the limit of the function in the first line of (33). The remaining partial derivatives with respect to ν_p , $|h_p|$, and $\angle h_p$ are straightforward and are omitted due to the lack of space. Finally, the CRB for the delay and Doppler parameters are computed as

$$\begin{aligned} \text{CRB}_{\text{delay}} &= [\mathbf{I}(\boldsymbol{\Theta})^{-1}]_{1+pP, 1+pP} \\ \text{CRB}_{\text{Doppler}} &= [\mathbf{I}(\boldsymbol{\Theta})^{-1}]_{2+pP, 2+pP}. \end{aligned} \quad (26)$$

C. FFT-based 2D Channel Estimation, Targets Branch

1) *OFDM*: The channel $\hat{\mathbf{H}}_{\text{ofdm}} \in \mathbb{C}^{M \times K}$ is estimated as

$$\begin{aligned} \hat{\mathbf{H}}_{\text{ofdm}} &= \mathbf{F}_M^H (\mathbf{F}_K^H ((\mathbf{F}_K \mathbf{Y}_{\text{ofdm}}) \odot \mathbf{D}_t))^T \\ &\approx \sum_{p=0}^{P-1} h'_p \mathbf{v}_{M, \tilde{\nu}_p} \mathbf{g}_{K, \tilde{\tau}_p}^T + \mathbf{W}'_{\text{los}} + \mathbf{W}'_{\text{ofdm}}. \end{aligned} \quad (27)$$

A proof that (27) holds is provided in Appendix B for completeness. Also, we note because the OFDM targets and LoS streams, $s_t(t)$ and $s_{\text{los}}(t)$, have different data symbols, the LoS interference component \mathbf{W}'_{los} in (27) becomes convoluted. Moreover, in this paper we do not evaluate the LoS interference removal for OFDM, thus we keep \mathbf{W}'_{los} without its explicit formulation for simplicity. The matrix $\mathbf{D}_t = [\mathbf{d}_{t_0} \ \mathbf{d}_{t_1} \ \cdots \ \mathbf{d}_{t_{M-1}}] \in \mathbb{C}^{K \times M}$ stacks the QAM sub-blocks along rows. The vector $\mathbf{v}_{M, \tilde{\nu}_t} \in \mathbb{C}^M$

$$\mathbf{v}_{M, \tilde{\nu}} = \mathbf{F}_M^H \mathbf{u}_{M, \tilde{\nu}} \quad (28)$$

is simply the inverse discrete Fourier Transform (IDFT) of the complex exponential containing the Doppler phase $\mathbf{u}_{M, \tilde{\nu}}[m] = \exp(-j2\pi\tilde{\nu}m/M)$. Intuitively, one can easily note that for integer values of the normalized Doppler $\tilde{\nu} = 0, \pm 1, \pm 2, \dots$, the IDFT $\mathbf{v}_{M, \tilde{\nu}}[m] = \sqrt{M}$ for $m = \pm\tilde{\nu}$ and 0 otherwise², which allows an estimation of the Doppler shift. Since the noise is divided by the QAM symbols in the frequency domain in (27), its power is $\tilde{\sigma}_w^2 = \sigma_w^2 \mathbb{E}(1/(dd^H)) = \sigma_w^2 L_{\text{ofdm}}$ for all (m, k) , in which

$$L_{\text{ofdm}} = \frac{1}{|\mathcal{S}|} \sum_{d \in \mathcal{S}} \frac{1}{dd^H}, \quad (29)$$

being \mathcal{S} the QAM set. Since $L_{\text{ofdm}} \geq 1$, with $L_{\text{ofdm}} = 1$ when $dd^H = 1 \forall d$, L_{ofdm} can be interpreted as the SNR loss in relation to the constant amplitude pilot signaling.

Lastly, it is worth noting that the operation of (27) is similar to the symplectic finite Fourier transform (SFFT) carried out in DD processing in OTFS. But here we have derived it with

²A proper FFT shift operation needs to be done to account for negative $\tilde{\nu}$.

equalization in the frequency domain outside the scope of OTFS. This enables a common framework for the UW frames of Subsection II-A.

2) *PS*: The estimator for the PS frame is similar to the CP-OFDM case, but the input is $\mathbf{Y}_{\text{ps}} \in \mathbb{C}^{K \times M_p}$ in (16) so that the estimated channel is

$$\begin{aligned} \hat{\mathbf{H}}_{\text{ps}} &= \mathbf{F}_{M_p}^H (\mathbf{F}_K^H ((\mathbf{F}_K \mathbf{Y}_{\text{ps}}) \odot \mathbf{P}))^T \\ &\approx \sum_{p=0}^{P-1} h'_p \mathbf{v}_{M_p, \tilde{\nu}_p} \mathbf{g}_{K, \tilde{\tau}_p}^T + \beta h'_{\text{los}} \mathbf{v}_{M_p, \tilde{\nu}_{\text{los}}} \mathbf{g}_{K, \tilde{\tau}_{\text{los}}}^T + \mathbf{W}'_{\text{ps}}, \end{aligned} \quad (30)$$

with size $\hat{\mathbf{H}}_{\text{ps}} \in \mathbb{C}^{M_p \times K}$. Analogously to \mathbf{D}_t in (27), $\mathbf{P} = [\mathbf{p}_0 \ \mathbf{p}_1 \ \cdots \ \mathbf{p}_{M_p-1}] \in \mathbb{C}^{K \times M_p}$ stacks the PS symbols along rows. And $\mathbf{v}_{M_p, \tilde{\nu}} = \mathbf{F}_{M_p}^H \mathbf{u}_{M_p, \tilde{\nu}}$ has size M_p . The power of \mathbf{W}'_{ps} is equal to σ_w^2 because \mathbf{p}_m has constant amplitude. Lastly, we note that the LoS interference has a convenient form because the pilot symbols are the same for both targets and LoS streams.

3) *UW1*: Following the same approach as the OFDM signaling, but with $\mathbf{Y}_{\text{uw1}} \in \mathbb{C}^{N_{\text{cp}} \times M}$ as input, the channel estimation for the UW1 signal is

$$\begin{aligned} \hat{\mathbf{H}}_{\text{uw1}} &= \mathbf{F}_M^H (\mathbf{F}_{N_{\text{cp}}}^H ((\mathbf{F}_{N_{\text{cp}}} \mathbf{Y}_{\text{uw1}}) \odot \mathbf{X}_{\text{uw1}}))^T \\ &\approx \sum_{p=0}^{P-1} h'_p \mathbf{v}_{M, \tilde{\nu}_p} \mathbf{g}_{N_{\text{cp}}, \tilde{\tau}_p}^T + \beta h'_{\text{los}} \mathbf{v}_{M, \tilde{\nu}_{\text{los}}} \mathbf{g}_{N_{\text{cp}}, \tilde{\tau}_{\text{los}}}^T + \mathbf{W}'_{\text{uw1}}, \end{aligned} \quad (31)$$

with size $\hat{\mathbf{H}}_{\text{uw1}} \in \mathbb{C}^{M \times N_{\text{cp}}}$, where $\mathbf{X}_{\text{uw1}} = \mathbf{F}_{N_{\text{cp}}} [\mathbf{x}_{\text{uw1}} \ \mathbf{x}_{\text{uw1}} \ \cdots \ \mathbf{x}_{\text{uw1}}] \in \mathbb{C}^{N_{\text{cp}} \times M}$ stacks the UW1 of size N_{cp} in frequency-domain along rows, with the time-domain raised cosine filter of size N_{cp} . Since the noise plus interference term \mathbf{W}_{uw1} in (25) is independent of the UW1, and the UW1 has constant amplitude in the frequency domain, it is easy to verify that the resulting noise plus interference \mathbf{W}'_{uw1} in (31) has the same power as \mathbf{W}_{uw1} , which is approximated by (17) with the SNR loss L_{uw1} given in (18).

4) *UW2*: Let the UW2 input be $\mathbf{Y}_{\text{uw2}} \in \mathbb{C}^{N_{\text{cp}}/2 \times M}$, the channel estimation is expressed as

$$\begin{aligned} \hat{\mathbf{H}}_{\text{uw2}} &= \mathbf{F}_M^H (\mathbf{F}_{N_{\text{cp}}/2}^H ((\mathbf{F}_{N_{\text{cp}}/2} \mathbf{Y}_{\text{uw2}}) \odot \mathbf{X}_{\text{uw2}}))^T \\ &\approx \sum_{p=0}^{P-1} h'_p \mathbf{v}_{M, \tilde{\nu}_p} \mathbf{g}_{N_{\text{cp}}/2, \tilde{\tau}_p}^T + \beta h'_{\text{los}} \mathbf{v}_{M, \tilde{\nu}_{\text{los}}} \mathbf{g}_{N_{\text{cp}}/2, \tilde{\tau}_{\text{los}}}^T + \mathbf{W}'_{\text{uw2}}, \end{aligned} \quad (32)$$

with size $\hat{\mathbf{H}}_{\text{uw2}} \in \mathbb{C}^{M \times N_{\text{cp}}/2}$, where $\mathbf{X}_{\text{uw2}} = \mathbf{F}_{N_{\text{cp}}/2} [\mathbf{x}_{\text{uw2}} \ \mathbf{x}_{\text{uw2}} \ \cdots \ \mathbf{x}_{\text{uw2}}] \in \mathbb{C}^{N_{\text{cp}}/2 \times M}$ stacks the UW2 signals of size $N_{\text{cp}}/2$ in frequency-domain along rows. In this case, the time-domain raised cosine filter has a size of $N_{\text{cp}}/2$. The power of \mathbf{W}'_{uw2} is equal to σ_w^2 because \mathbf{x}_{uw2} has constant amplitude.

$$\tilde{g}'_{\text{RC}}(t) = \frac{d\tilde{g}_{\text{RC}}(t)}{dt} = \begin{cases} \frac{1}{t} \frac{\cos(\alpha\pi t)(\cos(\pi t) - \text{sinc}(t))}{1 - (2\alpha t)^2} + \frac{8\alpha^2 t \cos(\alpha\pi t) \text{sinc}(\pi t)}{(1 - (2\alpha t)^2)^2} - \frac{\alpha\pi \sin(\alpha\pi t) \text{sinc}(\pi t)}{1 - (2\alpha t)^2}, & t \neq 0, t \neq \pm 1/(2\alpha) \\ 0, & t = 0 \\ 1/2\alpha (\pi \cos(\pi/(2\alpha)) - 3\alpha \sin(\pi/(2\alpha))), & t = \pm 1/(2\alpha) \end{cases} \quad (33)$$

D. LoS Channel Estimation

An analogous formulation for the LoS branch in Fig. 1 is straightforward to obtain by following the same steps of the previous subsection. As an example, the estimated LoS for the UW2 frame is

$$\hat{\mathbf{H}}_{\text{losuw2}} \approx \sum_{p=0}^{P-1} h'_{\text{los}} \mathbf{v}_{M, \hat{\nu}_{\text{los}}} \mathbf{g}_{N_{\text{cp}}/2, \hat{\tau}_{\text{los}}}^T + \mathbf{W}'_{\text{losuw2}}. \quad (34)$$

The other frames can be obtained by an analogous formulation. The interference from the target reflections into the LoS branch is incorporated in $\mathbf{W}'_{\text{losuw2}}$ for simplicity, and it is assumed to be negligible due to the much higher gain of the LoS path in comparison to the paths associated to the targets.

E. Fine Grid DD Estimation

Firstly, we define the DD signature matrix for the channel estimation schemes of Subsection IV-C as

$$\Psi_{\hat{\nu}, \hat{\tau}} = \begin{cases} \mathbf{v}_{M, \hat{\nu}} \mathbf{g}_{K, \hat{\tau}}^T, & \text{OFDM} \\ \mathbf{v}_{M_p, \hat{\nu}} \mathbf{g}_{K, \hat{\tau}}^T, & \text{PS} \\ \mathbf{v}_{M, \hat{\nu}} \mathbf{g}_{N_{\text{cp}}, \hat{\tau}}^T, & \text{UW1} \\ \mathbf{v}_{M, \hat{\nu}} \mathbf{g}_{N_{\text{cp}}/2, \hat{\tau}}^T, & \text{UW2} \end{cases}. \quad (35)$$

In the following we provide an iterative multi-user estimator similar to [15] where the estimates are refined by removing the interference from the targets. When the DD estimates for the LoS and the q th target are available $\{\hat{\nu}_q, \hat{\tau}_q\}$, their interference can be removed as

$$\hat{\mathbf{H}}_p = \hat{\mathbf{H}} - \sum_{\substack{q=0 \\ q \neq p}}^{P-1} \hat{h}'_q \Psi_{\hat{\nu}_q, \hat{\tau}_q} - (\widehat{\beta h'_{\text{los}}}) \Psi_{\hat{\nu}_{\text{los}}, \hat{\tau}_{\text{los}}}, \quad (36)$$

which is valid for PS, UW1 and UW2 and not for OFDM since its LoS interference has a different structure. Then, using the 2D channel estimation as the observation, the estimator for the p th DD target is given as

$$\{\hat{\nu}_p, \hat{\tau}_p\} = \max_{\hat{\nu}, \hat{\tau}} \frac{\left| \sum_{m,k} \hat{\mathbf{H}}_p[m, k] \Psi_{\hat{\nu}, \hat{\tau}}[m, k]^\dagger \right|^2}{\sum_{m,k} |\Psi_{\hat{\nu}, \hat{\tau}}[m, k]|^2}, \quad (37)$$

and the channel gain is estimated as

$$\hat{h}'_p = \frac{\hat{\mathbf{H}}_p[\text{round}(\hat{\nu}_p), \text{round}(\hat{\tau}_p)]}{\Psi_{\hat{\nu}_p, \hat{\tau}_p}[\text{round}(\hat{\nu}_p), \text{round}(\hat{\tau}_p)]}, \quad (38)$$

where the channel gain and phase of the p th target is estimated to allow proper removal in (36). Since the channel estimate $\hat{\mathbf{H}}_p$ is discrete, the DD estimated $\{\hat{\nu}_p, \hat{\tau}_p\}$ are approximated to the nearest integer to take the peak sample and avoid taking noisy samples in the channel gain estimation. Likewise, the LoS DD is estimated as

$$\{\hat{\nu}_{\text{los}}, \hat{\tau}_{\text{los}}\} = \max_{\hat{\nu}, \hat{\tau}} \frac{\left| \sum_{m,k} \hat{\mathbf{H}}_{\text{los}}[m, k] \Psi_{\hat{\nu}, \hat{\tau}}[m, k]^\dagger \right|^2}{\sum_{m,k} |\Psi_{\hat{\nu}, \hat{\tau}}[m, k]|^2}, \quad (39)$$

and the channel gain is estimated as

$$(\widehat{\beta h'_{\text{los}}}) = \frac{\hat{\mathbf{H}}[\text{round}(\hat{\nu}_{\text{los}}), \text{round}(\hat{\tau}_{\text{los}})]}{\Psi_{\hat{\nu}_{\text{los}}, \hat{\tau}_{\text{los}}}[\text{round}(\hat{\nu}_{\text{los}}), \text{round}(\hat{\tau}_{\text{los}})]}. \quad (40)$$

Algorithm 1 Multi-Target Delay-Doppler Estimation

- 1: Estimate $\hat{\mathbf{H}}$ according to Subsection IV-C
 - 2: Estimate $\hat{\mathbf{H}}_{\text{los}}$ according to Subsection IV-D
 - 3: Estimate $\{\hat{\nu}_{\text{los}}, \hat{\tau}_{\text{los}}\}$ with (39)
 - 4: Estimate $(\widehat{\beta h'_{\text{los}}})$ with (40)
 - 5: $\hat{h}'_p \leftarrow 0, \hat{\nu}_p \leftarrow 0, \hat{\tau}_p \leftarrow 0 \forall p$
 - 6: **for** $n_i = 1, \dots, N_{\text{iterations}}$ **do**
 - 7: **for** $p = 1, \dots, P$ **do**
 - 8: Estimate $\hat{\mathbf{H}}_p$ with (36)
 - 9: Estimate $\{\hat{\nu}_p, \hat{\tau}_p\}$ with (37)
 - 10: Estimate \hat{h}'_p with (38)
 - 11: **end for**
 - 12: **end for**
 - 13: Compute $\hat{\tau}_{\Delta_p} \leftarrow \hat{\tau}_p - \hat{\tau}_{\text{los}}$ and $\hat{\nu}_{\Delta_p} \leftarrow \hat{\nu}_p - \hat{\nu}_{\text{los}} \forall p$
-

Notice that the LoS branch is used to estimate the LoS DD $\{\hat{\nu}_{\text{los}}, \hat{\tau}_{\text{los}}\}$ in (39). Then, the interference gain is computed in (40) using the estimated channel in the targets branch so that it can be removed accordingly in (36). Furthermore, we highlight that the computation of (37) and (39) is implemented via a fine grid search whose complexity increases linearly with the desired grid resolution, thereby yielding the name *Fine Grid* estimator. The pseudocode for the multi-target DD estimation is presented in Algorithm 1, where the last step, line 13, is responsible for the offset cancellation in the delay and Doppler domains.

Lastly, we highlight that the presented algorithm relies on the assumption of a single path per target of (10). If each target produces multiple paths with a small delay and Doppler spread, the performance tends to degrade. This analysis is left for future work.

V. OUTLIER PROBABILITY OF INTEGER GRID ESTIMATOR

A. Integer Grid Estimator

In practical systems, the maximum likelihood or fine grid estimators of (20) and (37) might not be available for several reasons. For example, its complexity can be prohibitive, and the knowledge of the filter responses is not perfect making its implementation more difficult and less effective. Thus, a more practical solution is the estimation of the *Integer Grid* as

$$\{\hat{m}, \hat{k}\} = \max_{m,k} |\hat{\mathbf{H}}[m, k]|^2. \quad (41)$$

In this work, we focus on the outlier probability for the single-target case for simplicity, thus we keep the formulation (41) for this case. A generalization for the multiple targets case is possible by taking into account the mutual interference that the targets impose in each other. The sets \mathcal{M} and \mathcal{K} contain possible Doppler and delay indexes depending on the transmitted frame

$$\mathcal{K} = \begin{cases} \{0, 1, \dots, N_{\text{cp}} - 1\}, & \text{OFDM, PS \& UW1} \\ \{0, 1, \dots, N_{\text{cp}}/2 - 1\}, & \text{UW2} \end{cases} \quad (42)$$

and

$$\mathcal{M} = \begin{cases} \{0, 1, \dots, M - 1\}, & \text{OFDM, UW1 \& UW2} \\ \{0, 1, \dots, M_p\}, & \text{PS} \end{cases}. \quad (43)$$

B. Outlier Probability

By decoupling the DD into its integer and fractional components, a convenient metric to assess the performance of (41) is the outlier probability, which measures the probability that the integer DD estimation is wrong. Defining the DD by its integer and fractional components as $\tilde{\tau} = \tau_I + \tau_F$ and $\tilde{\nu} = \nu_I + \nu_F$, the 2D indexes that are mapped to the integer DD are $k_0 = \tau_I$ for the time index, and $m_0 = \nu_I$ if $\nu_I < M/2$ and $m_0 = M - \nu_I$ if $\nu_I \geq M/2$ for the Doppler index. Notice that a simple transformation is needed to account for negative Doppler.

The delay outlier probability for the delay estimation can be approximated by

$$P_{\text{delay}} \approx \Pr \left(\bigcup_{\substack{k \in \mathcal{K} \\ k \neq k_0}} \left\{ |\hat{\mathbf{H}}[m_0, k]| > |\hat{\mathbf{H}}[m_0, k_0]| \right\} \right) \\ \lesssim \sum_{\substack{k \in \mathcal{K} \\ k \neq k_0}} \Pr(|\hat{\mathbf{H}}[m_0, k]| > |\hat{\mathbf{H}}[m_0, k_0]|). \quad (44)$$

The first line of (44) computes the delay outlier probability assuming that the Doppler index is correctly estimated, where \mathcal{K} is given in (42). In particular, the event $|\hat{\mathbf{H}}[m_0, k]| > |\hat{\mathbf{H}}[m_0, k_0]|$ for an arbitrary $k \neq k_0$ indicates a situation where the estimator (41) would choose the wrong index k instead of k_0 . Since this can happen for multiple $k \neq k_0$, the outlier probability formulation takes the union of the events for all $k \neq k_0$. The second line is the well-known union bound or Boole's inequality, which counts the events' intersections more than once. For the Doppler estimation, the analogous formulation is

$$P_{\text{Doppler}} \lesssim \sum_{\substack{m \in \mathcal{M} \\ m \neq m_0}} \Pr(|\hat{\mathbf{H}}[m, k_0]| > |\hat{\mathbf{H}}[m_0, k_0]|), \quad (45)$$

where the delay index is assumed to be correctly estimated and \mathcal{M} is given in (43).

We note the absolute value of the channel estimate $|\hat{\mathbf{H}}[m, k]|$ in (44) and (45) follows a Rician distribution. Let $R \sim \text{Rice}(v, \sigma)$ be a Rician random variables with parameters (v, σ) and probability density function (PDF) given by

$$f_R(r; v, \sigma) = \frac{r}{\sigma^2} \exp\left(-\frac{(r+v)^2}{2\sigma^2}\right) I_0\left(\frac{rv}{\sigma^2}\right), \quad (46)$$

where $I_0(\cdot)$ is the modified Bessel function of the first kind with order zero. We have $|\hat{\mathbf{H}}[m, k]| \sim \text{Rice}(v_{m,k}, \sigma)$ with

$$v_{m,k} \approx |h\Psi_{\tilde{\nu}, \tilde{\tau}}[m, k]|, \quad (47)$$

and

$$\sigma^2 = \begin{cases} 1/2\sigma_w^2 L_{\text{ofdm}}, & \text{CP-OFDM} \\ 1/2\sigma_w^2, & \text{PS} \\ 1/2\sigma_w^2 L_{\text{uw1}}, & \text{UW1} \\ 1/2\sigma_w^2, & \text{UW2} \end{cases}, \quad (48)$$

where $\Psi_{\tilde{\nu}, \tilde{\tau}}$ and is given by (35). Thus, the problem of computing (44) and (45) consists of computing the probability that a Rician random variable (RV) is greater than another Rician RV, which is presented in the following.

C. Probability that a Rician Variable is Greater than Another

Let $X \sim \text{Rice}(v_x, \sigma)$ and $Y \sim \text{Rice}(v_y, \sigma)$ be independent Rician random variables with PDF given by (46). We are interested in computing the probability that X is greater than Y , which can be written using the cumulative distribution function (CDF) of the ratio X/Y by writing $\Pr(X > Y) = \Pr(X/Y > 1)$. The CDF of the ratio of independent Rician random variables has been derived in [29], and is given in (52) at the bottom of this page, where ${}_2F_1(\cdot, \cdot; \cdot; \cdot)$ is Gauss hypergeometric function.

Unfortunately, the numerical computation of (52) is not feasible in general due to the summations to infinity. To solve this issue, we provide two alternative solutions to compute (52) approximately with affordable complexity.

1) *Empirical Approximation (low and medium SNR)*: For simplicity, we first normalize $X' = X/\sigma \sim \text{Rice}(v'_x, 1)$ and $Y' = Y/\sigma \sim \text{Rice}(v'_y, 1)$, with $v'_x = v_x/\sigma$ and $v'_y = v_y/\sigma$. Clearly, $\Pr(X > Y) = \Pr(X' > Y')$.

By fixing v'_x and computing $\Pr(X > Y)$ for different values of v'_y with $v'_y > v'_x$, we realize that the resulting function behaves approximately as the Gaussian function, whose parameters depend on v'_x . Our approach is to compute the Gaussian parameters for some specific values of v'_x using (52) and then fit these values to a function such that a general expression is derived. The result is given below

$$\Pr(X > Y) \approx \begin{cases} \frac{1}{2} \exp\left(\frac{(v'_x - f_2(v'_x))^2 - (v'_y - f_2(v'_x))^2}{2f_1(v'_x)}\right), & v_x < v_y \\ 1 - \frac{1}{2} \exp\left(\frac{(v'_x - f_2(v'_x))^2 - (v'_y - f_2(v'_x))^2}{2f_1(v'_x)}\right), & v_x \geq v_y \end{cases} \quad (49)$$

where

$$f_1(v) = 2 + 0.6616(1 - \exp(-1.909v^{1.3838}))(1 + 1.909v^{1.3838}) \quad (50)$$

$$f_2(v) = 1.4899 \exp\left(-\frac{1}{0.39899v^{0.89899}}\right) v^{0.89899}. \quad (51)$$

Basically, (49) has the Gaussian function format over v'_y . This function has been normalized to satisfy $\Pr(X > Y) = 1/2$ if $v'_y = v'_x$. The functions $f_1(v)$ and $f_2(v)$ are the fitting functions having v'_x as input, which were found numerically. This solution is a very good approximation for $0 \leq v'_x < 30$. For $v'_x > 30$, the functions $f_1(v)$ and $f_2(v)$ do not approximate well the Gaussian function (49). By realizing that high values of v'_x imply high SNR, another approximation is possible in this regime which is studied in the following.

$$\Pr(X > Y) = \Pr(X/Y > 1) = \frac{1}{2} \exp\left(-\frac{v_x^2 + v_y^2}{2\sigma^2}\right) \sum_{k=0}^{\infty} \frac{1}{k!} \left(\frac{v_x^2}{2\sigma^2}\right)^k \sum_{j=0}^{\infty} \frac{1}{j!} \left(\frac{v_y^2}{4}\right)^j {}_2F_1\left(-j, -j; k+1; \frac{v_x^2}{v_y^2}\right) \quad (52)$$

TABLE I
COMPARISON OF THE FRAMES OF SUBSECTION II-A. INTEGER DD RESOLUTION, $\Delta_\tau = T_s$, AND $\Delta_\nu = B/N_x$.

Frame Design	Knowledge of Data, \mathbf{d}	Data Rate Loss	Proc. Gain	Complexity	Max. Delay	Maximum Abs. Doppler	SNR Loss
OFDM	yes	0	MK	$MK(\log_2 MK^2 + 1 + N_{\text{fg}})$	$(N_{\text{cp}} - 1)\Delta_\tau$	$(M/2 - 1)\Delta_\nu$	(29) & Table II
PS	no	M_p/M	$M_p K$	$M_p K(\log_2 M_p K^2 + 1 + N_{\text{fg}})$	$(N_{\text{cp}} - 1)\Delta_\tau$	$(M_p/2 - 1)\Delta_\nu$	no loss
UW1	no	0	MN_{cp}	$MN_{\text{cp}}(\log_2 MN_{\text{cp}}^2 + 1 + N_{\text{fg}})$	$(N_{\text{cp}} - 1)\Delta_\tau$	$(M/2 - 1)\Delta_\nu$	(18)
UW2	no	0	$M \frac{N_{\text{cp}}}{2}$	$M \frac{N_{\text{cp}}}{2} (\log_2 M (\frac{N_{\text{cp}}}{2})^2 + 1 + N_{\text{fg}})$	$(\frac{N_{\text{cp}}}{2} - 1)\Delta_\tau$	$(M/2 - 1)\Delta_\nu$	no loss

2) *Gaussian Approximation (high SNR)*: Again we consider $\Pr(X > Y) = \Pr(X/Y > 1)$. Next, we note that for high values of $v_x/(2\sigma^2)$ and $v_y/(2\sigma^2)$, X and Y approximate to Gaussian with low coefficients of variation $\delta_x = \sqrt{\mathbb{V}(X)}/\mathbb{E}(X)$ and $\delta_y = \sqrt{\mathbb{V}(Y)}/\mathbb{E}(Y)$, which is a condition for approximating the ratio X/Y to Gaussian as shown in [30]. Then, by letting $Z = X/Y$ be approximated to $\mathcal{N}(\mu_z, \sigma_z^2)$, its moments can be approximated as

$$\mu_z = \mathbb{E}(X/Y) \stackrel{(a)}{\approx} \mathbb{E}(X)/\mathbb{E}(Y) \stackrel{(b)}{\approx} v_x/v_y \quad (53)$$

and

$$\begin{aligned} \sigma_z^2 &= \mathbb{V}(X/Y) \stackrel{(a)}{\approx} \left(\frac{\mathbb{E}(X)^2}{\mathbb{E}(Y)^2} \right) \left(\frac{\mathbb{V}(X)^2}{\mathbb{E}(X)^2} + \frac{\mathbb{V}(Y)^2}{\mathbb{E}(Y)^2} \right) \\ &\stackrel{(c)}{\approx} v_x^2/v_y^2 (2\sigma^2/v_x^2 + 2\sigma^2/v_y^2). \end{aligned} \quad (54)$$

The approximations (a) in (53) and (54) use the method of [31, Example 5.5.27] by expanding the parametric function $g(X, Y) = X/Y$ around the mean of X and Y using the first-order Taylor series for both variables. The approximation (b) in (53) is attained due to $\mathbb{E}(X), \mathbb{E}(Y) \rightarrow v_x, v_y$ as $v_x, v_y \rightarrow \infty$, which becomes more accurate as v_x and v_y increases. The approximation (c) in (54) is attained due to $\mathbb{V}(X), \mathbb{V}(Y) \rightarrow 1$ as $v_x, v_y \rightarrow \infty$, which also becomes more accurate as v_x and v_y increases. Finally, we have

$$\Pr(X > Y) = \Pr(X/Y > 1) \approx Q\left(\frac{1 - \mu_z}{\sigma_z}\right), \quad (55)$$

where $Q(x) = \frac{1}{2} \int_x^\infty e^{-t^2/2} dt$. This approximation is used for $v_x' \geq 30$.

VI. FRAME DESIGN OVERVIEW

In this section, we provide a comparative overview of the frames described in Subsection II-A. The parameters analyzed in this section are described in Table I.

The idea of using PS, UW1, and UW2 processing is to avoid the need for the passive radar unit to know the transmitted data \mathbf{d} , to facilitate the deployment. Another relevant aspect is the loss in data rate when dedicated pilot symbols replace the OFDM sub-blocks, which happens in the PS frame type. Since the PS frame spends M_p out of M for the pilots, its data rate loss is given by M_p/M . The above considerations are indicated in Table I and illustrate well the motivation behind considering the UW1 and UW2 frames, which simultaneously avoid the radar's need to know the data, and do not incur data rate loss for communications.

The remaining quantitative parameters are analyzed in the following subsections.

A. Processing Gain

The processing gain is a typical radar parameter related to the gain in SNR due to coherent processing, which is proportional to the number of time-domain samples processed by the radar receiver. For the passive radar schemes considered in this paper, the processing gain is exactly the number of samples per sub-block times the number of sub-blocks. Then, the processing gain for each frame scheme is given by $G_{\text{ofdm}} = MK$, $G_{\text{ps}} = M_p K$, $G_{\text{uw1}} = MN_{\text{cp}}$ and $G_{\text{uw2}} = MN_{\text{cp}}/2$.

B. Delay-Doppler Resolution

The *Integer Grid* delay-Doppler resolution is the same for all frames, namely, $\Delta_\tau = T_s = 1/B$ for time and $\Delta_\nu = B/N_x$ for Doppler, and is valid for single and multiple targets. The time resolution is simply the sampling interval. For the Doppler resolution, it is the subcarrier spacing when the whole bandwidth is divided by the total number of transmitted samples $N_x = M(N_{\text{cp}} + K)$, which is the same for all frames. Note that what differentiates the frames of Subsection IV-C is the samples in which the radar receiver processes, while the transmitted frames have all the same format in terms of size and number of sub-blocks.

The resolution for the *Fine Grid* estimator is simply the *Integer Grid* resolution divided by the number of times the *Integer Grid* is partitioned.

C. Maximum Unambiguous Delay-Doppler

The maximum delay-Doppler is the resolution multiplied by the maximum index of the *Integer Grid*. For the delay, these numbers are $\tau_{\text{ofdm}}^{\text{max}} = \tau_{\text{ps}}^{\text{max}} = \tau_{\text{uw1}}^{\text{max}} = (N_{\text{cp}} - 1)\Delta_\tau$, $\tau_{\text{uw2}}^{\text{max}} = (N_{\text{cp}}/2 - 1)\Delta_\tau$. The respective maximum absolute Doppler are $\nu_{\text{ofdm}}^{\text{max}} = \nu_{\text{uw1}}^{\text{max}} = \nu_{\text{uw2}}^{\text{max}} = (M/2 - 1)\Delta_\nu$, $\nu_{\text{ps}}^{\text{max}} = (M_p/2 - 1)\Delta_\nu$.

We observe that the PS frame has reduced maximum Doppler because its processed sub-blocks have a larger time separation, which causes an effect of increasing the channel sampling interval by M/M_p times in relation to the other frames. Also, the UW2 frame has reduced maximum delay because its equivalent CP size is half the size of the other frames.

D. Complexity of FFT-based Receiver

The complexity of the *Integer Grid* estimator is dictated by the channel estimation operation shown in the Subsection IV-C. And the *Fine Grid* estimator has additional costs to compute (37).

TABLE II
SNR LOSS OF OFDM.

QAM order	4	16	64	256	1024
L_{ofdm}	1	1.89	2.68	3.43	4.17
$10 \log_{10} L_{\text{ofdm}}$	0	2.76	4.29	5.36	6.2

1) *Channel Estimation, Subsection IV-C*: Taking the example of OFDM processing, the channel estimation requires $2|\mathcal{M}|$ FFTs of size $|\mathcal{K}|$, $|\mathcal{K}||\mathcal{M}|$ complex-valued multiplications to equalize the channel, and then $|\mathcal{K}|$ FFTs of size $|\mathcal{M}|$.

2) *Fine Grid Estimation, equation (37)*: to achieve a resolution of $1/N_{\text{grid}}$ about the integer grid estimates, the fine grid estimator (37) computes $|\mathcal{K}||\mathcal{M}|$ complex-valued multiplications $N_{\text{fig}} = 2N_{\text{iterations}}P \log_2 N_{\text{grid}}$ times for all targets and iterations of Algorithm 1. $N_{\text{iterations}}P$ are the number of outer iterations and targets. $2 \log_2 N_{\text{grid}}$ is because of a binary grid search that subdivides the grid by half in each step, and each step tests 2 candidates.

Taking $|\mathcal{K}|$ and $|\mathcal{M}|$ from (42) and (43), respectively, considering that the K -size FFT consumes $K \log_2 K$, the above complexities in terms of complex-valued multiplications are $O_{\text{ofdm}} = 2MK \log_2 K + KM + KM \log_2 M + N_{\text{fig}}KM = MK(\log_2 MK^2 + 1 + N_{\text{fig}})$, $O_{\text{ps}} = M_p K(\log_2 M_p K^2 + 1 + N_{\text{fig}})$, $O_{\text{uw1}} = N_{\text{cp}}M(\log_2 MN_{\text{cp}}^2 + 1 + N_{\text{fig}})$ and $O_{\text{uw2}} = MN_{\text{cp}}/2M(\log_2(N_{\text{cp}}/2)^2 + 1 + N_{\text{fig}})$.

Not surprisingly, the complexity scales with the number of samples to be processed, i.e., the processing gain, indicating a trade-off between processing gain and complexity. It is worth noting that

E. SNR Loss of FFT-based Receiver

It is convenient to work with the SNR after radar processing, which has the definition below

$$\rho = G|h|^2/\sigma_w^2, \quad (56)$$

for one target, where G is the processing gain and is given in Subsection VI-A for each frame.

For the OFDM frame, the SNR loss L_{ofdm} happens due to the non-constant amplitude signaling in the frequency domain. It is computed in equation (29), and the values for pertinent QAM constellation are given in Table II.

For the UW1 frame, the SNR loss is caused by the CP-restoration procedure, which superposes additional noise and OFDM symbol terms to the signal of interest. Combining (56) with the SNR loss given in (18), we find the formula

$$L_{\text{uw1}} = 2 + \rho/G_{\text{uw1}} + \beta^2|h_{\text{los}}|^2/\sigma_w^2. \quad (57)$$

As such, its signal-to-interference noise ratio (SINR) is given by

$$\rho_{\text{uw1}} = \rho / (2 + \rho/G_{\text{uw1}} + \beta^2|h_{\text{los}}|^2/\sigma_w^2) \approx \begin{cases} \rho/2, & \rho \ll G_{\text{uw1}} \text{ and } \beta^2|h_{\text{los}}|^2 \ll \sigma_w^2 \\ G_{\text{uw1}}, & \rho \gg G_{\text{uw1}} \text{ and } \beta^2|h_{\text{los}}|^2 \ll \sigma_w^2 \end{cases}, \quad (58)$$

where the second line is the asymptotic SINR without LoS interference in high and low SNR regimes. In particular, we can observe that in the low SNR regime, the SNR loss for

TABLE III
SIMULATION PARAMETERS FOR FIGS. 6, 7, 8 AND 9.

Param.	Value	Param.	Value
FFT size, K	128	CP size, N_{cp}	32
n. of sub-vectors, M	64	OFDM QAM order	256
n. of PS sub-vectors, M_p	8	roll-off factor, α	0.25

the UW1 frame is 2. In the high SNR region, the loss scales proportionally with the SNR before the radar processing. As a result, the maximum SINR after radar processing is G_{uw1} .

VII. NUMERICAL RESULTS

A. Delay-Doppler Estimation

In this subsection, we show the results related to the DD estimators shown in Section IV. In particular, the *Fine Grid* and *Integer Grid* estimators are evaluated via Monte Carlo simulations, which are described in Subsections IV-E and V-A, respectively. For benchmarking, the MLE of Subsection IV-A and the CRB of Subsection IV-B are evaluated. The parameters for this numerical evaluation are shown in Table III. The *Fine Grid* estimator described in Algorithm 1 divides the *Integer Grid* into 256 parts to compute (37) and (39) which is achieved by 8 binary refinement steps, which is enough resolution to guarantee a root mean square error (RMSE) normalized to the DD resolution under 10^{-2} at high SNR. The estimators are compared with the same radar SNR defined in (56) to allow an evaluation of the SNR loss of Table I. This means that the effect of the processing gain, or number of samples processed, is not observed in these plots. A high-level analysis is done in Subsection VII-C that takes into consideration the radar processing gain effects in terms of range.

Fig. 6 evaluates the RMSE of the radar normalized DD pair one target and $\beta = 0$, which are fixed to $\tilde{\tau} = 4.249$ and $\tilde{\nu} = 2.237$ to allow the CRB with the unknown fixed parameter. We first note that the MLEs meet the CRBs in a high SNR regime, indicating their accuracy. Moreover, the results reveal that UW2 and PS frames with the *Fine Grid* estimator achieve the ML. The reason is that the equalization does not incur loss nor does it change the noise statistics due to constant amplitude. For OFDM, we note that the SNR loss is $10 \log_{10} L_{\text{ofdm}} = 5.36$ for 256 QAM according to Table II when the *Fine Grid* estimator is employed. For the UW1 case, the extreme cases described by equation (58) are observed, namely, in the low radar SNR region, the SNR loss is 3 dB about the UW2 case. In the high SNR region, SINR stagnates at $G_{\text{uw1}} = N_{\text{cp}}M = 2048$. This can be observed in Fig. 6, where UW1 frame with the *Fine Grid* estimator displays a floor at high SNR. We also note that the waterfall region of OFDM and UW1 frames is shifted to the right. Even though their respective MLEs achieve the CRB, it happens at a higher SNR than the PS and UW2 frames, indicating their fundamental suboptimality. Lastly, the *Integer Grid* estimator achieves an RMSE exactly matching the fractional delay and Doppler which are 2.49×10^{-1} and 2.37×10^{-1} , respectively. This indicates that the *Integer Grid* estimator estimates the integer DD with high probability. A more detailed assessment in this regard is provided in the subsequent subsection.

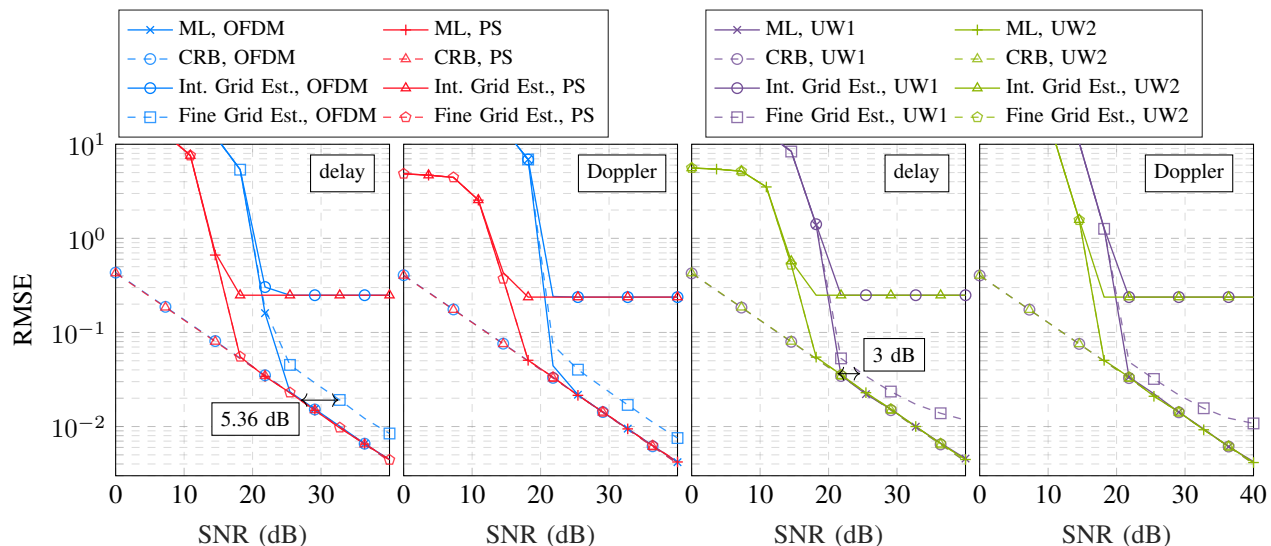


Fig. 6. Analysis of the single-target DD estimators of Section IV without LoS interference. The delay and Doppler are fixed, $\tilde{\tau} = 4.249$ and $\tilde{\nu} = 2.237$.

Fig. 7 evaluates the immunity that the UW1 and UW2 frames have concerning the LoS interference with a single target. The results show the RMSE of the difference $\hat{\tau}_{\Delta p} = \hat{\tau}_p - \hat{\tau}_{\text{los}}$ and $\hat{\nu}_{\Delta p} = \hat{\nu}_p - \hat{\nu}_{\text{los}}$, so that TO and CFO are compensated. This evaluation considers the LoS radar SNR of 50 dB, so that the LoS DD can be accurately estimated and is typically orders of magnitude larger than the target radar SNR. Three antenna rejection conditions are considered, namely, $\beta = \{0, 1/10, 1/\sqrt{2}\}$. The target delay and Doppler follows the uniform distribution $\tilde{\tau} \sim \mathcal{U}(3.5, 4.5)$ and $\tilde{\nu} \sim \mathcal{U}(1.5, 2.5)$, respectively. The LoS delay and frequency shift follow $\tilde{\tau}_{\text{los}} \sim \mathcal{U}(0, 0.5)$ and $\tilde{\nu}_{\text{los}} \sim \mathcal{U}(0, 0.1)$, respectively. The results reveal a high sensitivity of the UW1 system regarding the LoS interference when the antenna rejection is low. Specifically, for $\beta = 1/\sqrt{2}$ we have the term³ $\beta^2 |h_{\text{los}}|^2 / \sigma_w^2 = 24.41$ in (57) which sufficient to cause a significant performance loss. On the other hand, when $\beta = 1/10$ we have $\beta^2 |h_{\text{los}}|^2 / \sigma_w^2 = 0.49$ with negligible impact. Regarding the UW2 frame, it is considerably more resilient to high LoS interference, although it has some nonnegligible performance loss when the LoS is high, due to imperfect LoS interference removal as a product of the approximated model (19).

The multi-target delay difference estimation is evaluated in Fig. 8 with moderate LoS interference $\beta = 1/10$ with the same LoS model as the results of Fig. 7. This simulation considers two targets with equal radar SNRs with $N_{\text{iterations}} = 8$ in Algorithm 1. The first target, $p = 0$, has the same DD distribution as the one of Fig. 7, i.e., $\tilde{\tau}_0 \sim \mathcal{U}(3.5, 4.5)$, $\tilde{\nu}_0 \sim \mathcal{U}(1.5, 2.5)$. The second target, $p = 1$, has its DD as $\tilde{\tau}_1 = \tilde{\tau}_0 + \Delta_{\tilde{\tau}\tilde{\nu}}$ and $\tilde{\nu}_1 = \tilde{\nu}_0 + \Delta_{\tilde{\tau}\tilde{\nu}}$ for $\Delta_{\tilde{\tau}\tilde{\nu}} = \{0.5, 0.75, 1, 1.25\}$ so that we can evaluate the multi-target estimation capability for different fractional DD deviations. The results for $\Delta_{\tilde{\tau}\tilde{\nu}} = 0.5$ lead to a high floor in both frames, which is still lower than the one of the *Integer Grid* estimator when compared to the results of Fig. 6. As expected, the error floor decreases systematically as the deviation $\Delta_{\tilde{\tau}\tilde{\nu}}$ increases. For $\Delta_{\tilde{\tau}\tilde{\nu}} = 1.25$, both frames can

³The LoS radar SNR is 50 dB, meaning that $G_{\text{uw1}} |h_{\text{los}}|^2 / \sigma_w^2 = 10^5$ for $G_{\text{uw1}} = N_{\text{cp}} M = 2048$.

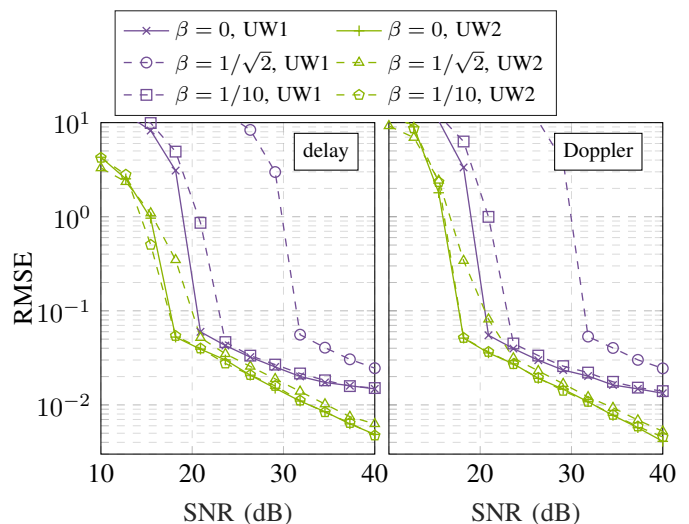


Fig. 7. RMSE with different values of β . The target DD are distributed as $\tilde{\tau} \sim \mathcal{U}(3.5, 4.5)$, $\tilde{\nu} \sim \mathcal{U}(1.5, 2.5)$, $\tilde{\tau}_{\text{los}} \sim \mathcal{U}(0, 0.5)$ and $\tilde{\nu}_{\text{los}} \sim \mathcal{U}(0, 0.1)$.

estimate both targets as accurately as possible. Here we note that the UW1 does not achieve the single target benchmark curve because it has more CP-restoration interference with $P = 2$ than with $P = 1$, as shown in (18).

B. Outlier Probability

This subsection investigates the outlier probability for one target and perfect LoS interference removal using the parameters of Table III to evaluate the outlier probability UBs (44) and (45). The results are shown in Fig. 9 in the next page, where the simulated outlier probability is also plotted. The first and second graph depicts the result for a fixed value of DD $(\tilde{\tau}, \tilde{\nu}) = (4.417, 2.405)$, while the third and fourth graphs have a more general case with integer DD $(\tilde{\tau}_1, \tilde{\nu}_1) = (4, 2)$ and fractional DD uniformly distributed between $-1/2$ and $1/2$, so that $\tilde{\tau} \sim \mathcal{U}(3.5, 4.5)$, $\tilde{\nu} \sim \mathcal{U}(1.5, 2.5)$. The UBs (44) and (45) become tight at relatively high SNR, as expected. They approach the simulation after the waterfall region when

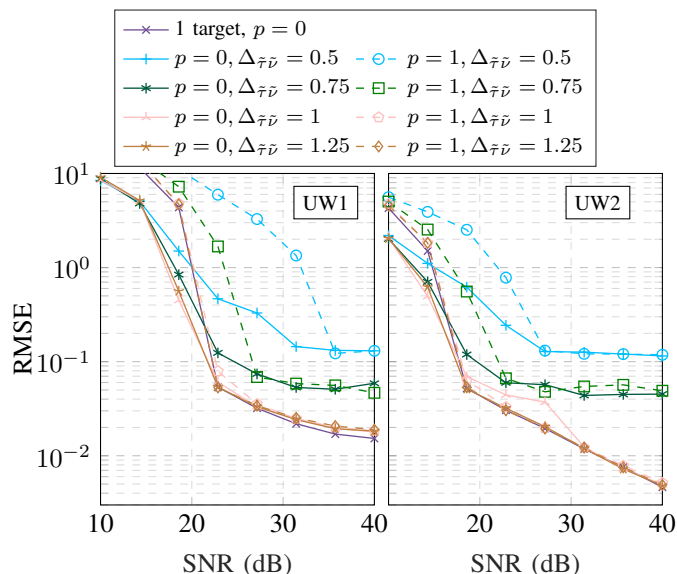


Fig. 8. Delay estimation for 2 targets with different fraction DD deviations $\Delta\bar{\tau}\bar{\nu}$. The target DDs are distributed as $\bar{\tau}_0 \sim \mathcal{U}(3.5, 4.5)$, $\bar{\nu}_0 \sim \mathcal{U}(1.5, 2.5)$, $\bar{\tau}_1 = \bar{\tau}_0 + \Delta\bar{\tau}\bar{\nu}$, $\bar{\nu}_1 = \bar{\nu}_0 + \Delta\bar{\tau}\bar{\nu}$, $\bar{\tau}_{\text{los}} \sim \mathcal{U}(0, 0.5)$ and $\bar{\nu}_{\text{los}} \sim \mathcal{U}(0, 0.1)$.

compared to the RMSE of Fig. 6. For the random fractional DD, we see that the outlier probability becomes less steep. This happens because there are some values of fractional DD that have relatively high peaks for $k \neq k_0$ and $m \neq m_0$, which increases the overall outlier probability.

Moreover, a useful waterfall region analysis is done with these outcomes, that is a region from a given SNR reference point where the RMSE and outlier probability drop considerably. Specifically, based on the results of Fig. 9, we can define an SNR beyond which an outlier probability of $P_{\text{delay}} \leq 5 \times 10^{-2}$ and $P_{\text{Doppler}} \leq 5 \times 10^{-2}$ is expected, which have tight outlier probability. For the PS and UW2 frames, this happens beyond 17 dB. For the OFDM frame, it happens after $17 + 10 \log_{10} L_{\text{ofdm}} = 22.36$ dB. For the UW1 frame, the limit is $17 + 3.01 = 20.01$ dB, since in the relatively low SNR region, the SNR loss for the UW1 frame is approximately 3.01 dB. These reference numbers are used in the range analysis performed in the subsequent subsection.

C. Range Comparison of Different Frame Schemes

This subsection provides a high-level range comparison between the OFDM, PS, UW1, and UW2 frames, for one target estimation and perfect LoS interference removal. The target channel model considered is the double-path loss

$$|h|^2 = \frac{PG_{\text{bs}}G_{\text{r}}\lambda^2\sigma_{\text{rcs}}}{(4\pi)^3(d_{\text{BT}}d_{\text{TR}})^\eta}, \quad (59)$$

with system level parameters are shown in Table IV, where d_{BT} is the distance between the BS and target, and d_{TR} is the distance between the target and radar. An illustration is depicted in the top graph of Fig. 10 with the bases station (BS), passive radar (PR), and target contours which are used in the range study in the remainder of this subsection.

Two configurations are considered, namely, outdoor and indoor. The outdoor configuration has the distance between

TABLE IV
SIMULATION PARAMETERS FOR FIG. 10.

Parameter	Outdoor	Indoor
OFDM SCS bandwidth, B	120 kHz	480 kHz
BS-radar distance, d_{BR}	200 m	20 m
radar RCS, σ_{rcs}	10 m ²	1 m ²
FFT size, K		1024
number of sub-vectors, M		140
number of PS sub-vectors, M_{p}		20
CP size, N_{cp}		204
OFDM QAM order		256
roll-off factor, α		0.25
center frequency, f_c		28 GHz
transmit power, P_{bs}		23.98 dBm
path loss exponent, η		2.3 [32]
BS antenna gain, G_{bs}		8
Radar antenna gain, G_{r}		64
noise PSD		-174 dBm/Hz

the BS and radar $d_{\text{BR}} = 200$ m and $\sigma_{\text{rcs}} = 10$ m². The indoor case has the distance between the BS and radar $d_{\text{BR}} = 20$ m and $\sigma_{\text{rcs}} = 1$ m². We note that the CP and UW sizes are 20% of the FFT size, which is a typical proportion. The CP duration N_{cp}/B equals 1627 ns and 406 ns for the outdoor and indoor environments, respectively. These are practical guard interval quantities for communications with a reasonable margin since the maximum delay in outdoor and indoor environments has been reported to be around 700 ns [33] and 200 ns [32] at 28 GHz, respectively. Lastly, we note that the UW frames offer $M_{\text{p}}/(M - M_{\text{p}}) \times 100 = 16.67\%$ more data than the PS frame.

In the following, we analyze the range from two relevant perspectives. The first is the maximum bistatic range based on the iso-range contour, where the maximum unambiguous delay in Table IV is considered. The second is the constant SNR Cassini oval where the waterfall SNRs for OFDM, PS, UW1, and UW2 are 22.36, 17, 20.03, and 17 dB, respectively. The details related to the iso-range contour and Cassini oval are given in Appendix C, and an illustration is depicted in the top graph of Fig. 10 for the outdoor setting.

The results are better compared with the middle and bottom graphs, where the distance between the target and radar, d_{TR} , for different angles θ_{TR} , are plotted matching the contours depicted in the graph at the top. We note that the distance between the BS and radar, d_{BR} , is plotted as black dashed line for reference. Firstly, we analyze the maximum unambiguous range of OFDM, PS, and UW1 in comparison to UW2. As expected, the range reduction of UW2 is evident due to its smaller maximum delay. In particular, for the outdoor configuration and $\theta_{\text{TR}} = 120^\circ$, $d_{\text{TR,max}} \approx 230$ m for the UW2 frame, while it is $d_{\text{TR,max}} \approx 375$ m for the other frames. It is interesting to note that although the maximum unambiguous delay of the UW2 frame is half the others, its maximum range is typically more than half of the other methods, demonstrating that the range reduction of UW2 is not as bad as one would expect.

Regarding the maximum distance that achieves the waterfall SNRs obtained via the Cassini oval, we observe that the difference between UW1 and UW2 frames is not very high from PS for both configurations. For example, for $\theta_{\text{TR}} = 120^\circ$, $d_{\text{TR,Cass.}} \approx 207$ m for the UW1 and UW2 frames, while it is

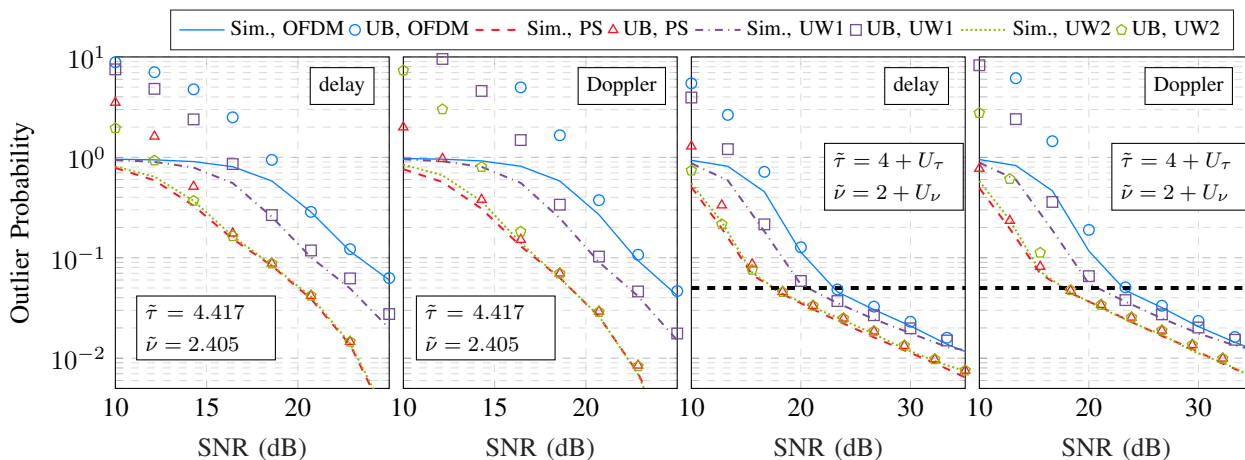


Fig. 9. Outlier probability. First and second graphs have fixed DD $(\tilde{\tau}, \tilde{\nu}) = (4.417, 2.405)$. Third and fourth graphs have integer DD $(\tilde{\tau}_1, \tilde{\nu}_1) = (4, 2)$ and fractional DD uniformly distributed between $-1/2$ and $1/2$, so that $\tilde{\tau} \sim \mathcal{U}(3.5, 4.5)$, $\tilde{\nu} \sim \mathcal{U}(1.5, 2.5)$.

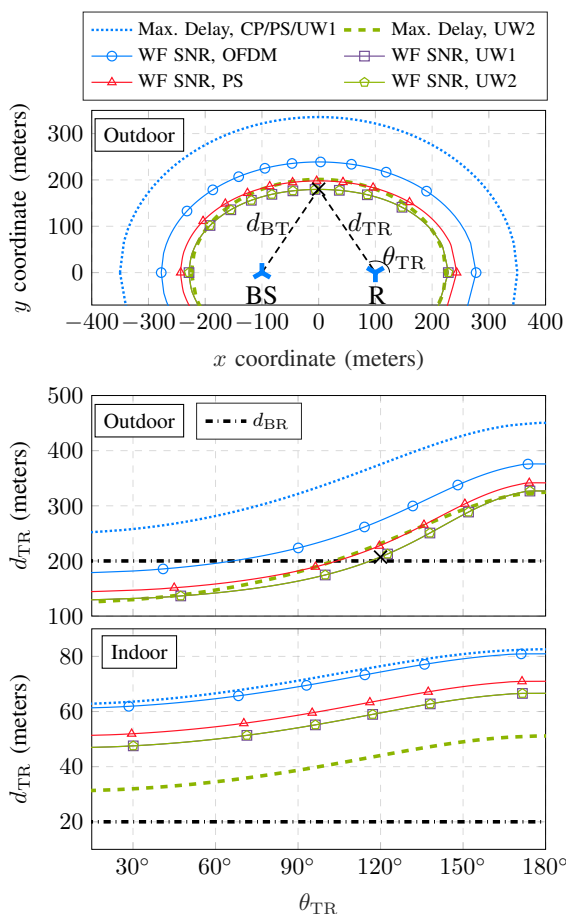


Fig. 10. Range comparison of the OFDM, PS, UW1, and UW2 frames. The top graph shows the Cassini oval and iso-range contours taking the radar as a reference. The middle and bottom graphs plot d_{TR} for different angles θ_{TR} . The waterfall (WF) SNRs for OFDM, PS, UW1, and UW2 are 22.36, 17, 20.03, and 17 dB, respectively.

approximately 228 m and 273 m for PS and OFDM, respectively. We note that the Cassini ovals are directly dependent on the processing gain and SNR loss of Table I. Since we can expect the UW1, UW2, and PS frames to have a similar processing gain for practical configurations, the Cassini ovals between the UW1, UW2, and PS frames will be similar in general. It is also possible that the UW1 and UW2 frames

have a broader Cassini oval than the PS for smaller values of M_p . This makes both UW frames to be a promising alternative to avoid sacrificing the data rate to realize sensing tasks. When comparing both UW frames, we see that they have very similar Cassini oval. This happens because the $2\times$ higher processing gain of UW1 is compensated by its $2\times$ SNR loss. Nevertheless, the UW1 frame suffers from an SNR floor which does not appear for the UW2 frame. Thus, when the unambiguous range is not critical, the UW2 frame is preferred.

For the indoor scenario, the Cassini oval is way beyond the maximum bistatic range, indicating that this case is limited by the CP size and not the power. Interestingly, the maximum bistatic range surpasses 30 m for the UW2 frame. Considering that the distance between the transmitter and the radar $d_{BR} = 20$ m, we can expect the maximum bistatic range to be sufficient even for the UW2 frame. Since the UW2 frame has a steeper estimation curve according to the results of Fig. 6, in this situation UW2 frame is more suitable than the UW1.

In summary, the UW1 and UW2 frames are competitive when compared to the PS design since they achieve similar performance without compromising the data rate for communications users. For outdoor scenarios where the maximum bistatic range is more relevant, the UW1 is a more suitable solution than the UW2. In indoor scenarios where the range is not critical, the UW2 frame is a more suitable solution when the *Fine Grid* FFT-based receiver is employed, since it does not have the error floor of the UW1 frame.

VIII. CONCLUSION

In this work, we have proposed two solutions for ISAC frame design for bistatic radar within mobile communication systems. Specifically, the idea consists of placing deterministic signals, based on the ZC sequence, into the guard interval instead of the CP. The first is the UW1 with the CP size. The second is two UWs with half of the CP size appended after each other, which is termed UW2. The performance of the proposed UW-based frames has been compared to OFDM and PS frames. Against OFDM, the UW frames are advantageous because they do not require the radar to know the data symbols, which is a requirement that can be impractical.

Concerning the PS, the UW solutions do not compromise the data rate for communication.

We have derived relevant theoretical results which have been validated by numerical analysis. Considering a band-limited system with an RRC filter, we have derived the CRB. In addition, we have derived an FFT-based multi-target delay-Doppler (DD) estimator with LoS interference removal, and the outlier probability computation when the integer part of the DD is erroneously estimated. Lastly, we have compare all methods in terms of sensing range. The UW2 has the drawback of decreasing the maximum unambiguous estimation range from 50% to 70%, which can be critical in outdoor sensing, but not so much for the indoor setting considered. In terms of the maximum range due to radar SNR, both UW waveforms have a very similar range to the PS system. In summary, the UW frames are good alternative candidates for bistatic ISAC, where the UW1 is more suitable for outdoor sensing, and the UW2 is more suitable for indoor.

There are several aspects to be further explored in future research, namely, i) explore the impact of clutter on the UW frames, ii) extend the model to perform angle-of-arrival estimation, which is also a typical parameter to be sensed, iii) explore the UW for line-of-sight synchronization, iv) enhance the unambiguous range of the UW2 method, and v) investigate the impact of multipath per target in the radar channel model.

APPENDIX

A. Discrete Time Signal Approximation

Considering only one target and no LoS interference for simplicity of the exposition, i.e., $\beta = 0$ and $P = 1$ in (10), the sampled OFDM signal is given by

$$\begin{aligned} \mathbf{Y}_{\text{ofdm}}[k, m] &= y_t(I_{\text{ofdm}}(k, m)T_s) \\ &\stackrel{(a)}{\approx} h e^{-j2\pi\nu I(k, m)T_s} \sum_{n=0}^{N_x-1} \mathbf{x}[n] g_{\text{RC}}((I(k, m) - n)T_s - \tau) \\ &\quad + w'_t(I(k, m)T_s) \\ &\stackrel{(b)}{\approx} h e^{-j2\pi\nu I(k, m)T_s} (\mathbf{x}_m \circledast \mathbf{g}_{K, \tilde{\tau}})[k] + \mathbf{W}[k, m] \\ &\stackrel{(c)}{\approx} h' \mathbf{u}_{M, \tilde{\nu}}[m] (\mathbf{x}_m \circledast \mathbf{g}_{K, \tilde{\tau}})[k] + \mathbf{W}[k, m], \end{aligned} \quad (60)$$

for $0 \leq k < K$ and $0 \leq m < M$ such that $\mathbf{Y}_{\text{ofdm}} \in \mathbb{C}^{K \times M}$. The index mapper $I_{\text{ofdm}}(k, m) = (k + N_{\text{cp}} + m(N_{\text{cp}} + K))$ is used to place the received signal associated with the m th sub-block in the m th column of \mathbf{Y}_{ofdm} , where the CP is removed to allow frequency domain processing. In (60), (a) represents the same approximation of (11). Line (b) writes a circular convolution between the discrete time signal \mathbf{x} and the raise-cosine filter normalized to the sampling interval

$$\mathbf{g}_{K, \tilde{\tau}}[k] = \tilde{g}_{\text{RC}}(k - \tilde{\tau}), \quad (61)$$

for $k = 0, 1, \dots, K - 1$, where $\tilde{g}_{\text{RC}}(t) = g_{\text{RC}}(t/T_s)$, $\tilde{\tau} = \tau/T_s$ is the delay normalized to the sampling interval, which is assumed to be in the interval $0 \leq \tilde{\tau} < N_{\text{cp}}$. The subscript K in (61) denotes its size. It is an approximation because the time-domain filter does not provoke a perfect circular convolution due to non-zero samples being larger than

the CP size. Lastly, the approximation in (c) considers that the term $e^{-j2\pi\nu I(k, m)T_s}$ remains approximately constant within the period of the m th sub-block with phase

$$\mathbf{u}_{M, \tilde{\nu}}[m] = \exp(-j2\pi\tilde{\nu}m/M), \quad (62)$$

where $\tilde{\nu} = \nu T_s N_x$ is the frequency shift normalized to subcarrier spacing of the whole signal if the bandwidth is divided by N_x . In practice, (c) tends to be less accurate as K increases because it could lead to significant phase changes within a sub-block. The channel coefficient denoted by h' takes into account the appropriate initial phase.

The approximation shown in (15) is obtained by combining (60) with the multiple targets and LoS interference of (10).

B. 2D Channel Estimation

In the following, we show that $\hat{\mathbf{H}}_{\text{ofdm}} \in \mathbb{C}^{M \times K}$ of (27) holds. Neglecting the LoS interference, and start with the single target assumption, we have

$$\hat{\mathbf{H}}_{\text{ofdm}} = \mathbf{F}_M^H (\mathbf{F}_K^H ((\mathbf{F}_K \mathbf{Y}_{\text{ofdm}}) \circledast \mathbf{D}))^T \approx h' \mathbf{v}_{M, \tilde{\nu}} \mathbf{g}_{K, \tilde{\tau}}^T + \mathbf{W}'. \quad (63)$$

Let $\mathbf{g}_{K, M, \tilde{\tau}} = [\mathbf{g}_{K, \tilde{\tau}} \ \mathbf{g}_{K, \tilde{\tau}} \cdots \mathbf{g}_{K, \tilde{\tau}}] \in \mathbb{R}^{K \times M}$ be the normalized raised cosine filter replicated M times along columns, and $\mathbf{u}_{M, K, \tilde{\nu}} = [\mathbf{u}_{M, \tilde{\nu}} \ \mathbf{u}_{M, \tilde{\nu}} \cdots \mathbf{u}_{M, \tilde{\nu}}] \in \mathbb{R}^{M \times K}$ be the Doppler phase shift replicated K times along columns. Ignoring the noise component and the channel phase h' in (15), we first note that $\mathbf{F}_K \mathbf{Y}_{\text{ofdm}} \approx (\mathbf{u}_{M, K, \tilde{\nu}})^T \circledast \mathbf{G}_{K, M, \tilde{\tau}} \circledast \mathbf{D}$, where $\mathbf{G}_{K, M, \tilde{\tau}} = \mathbf{F}_K \mathbf{g}_{K, M, \tilde{\tau}}$ and \mathbf{D} are the data symbols stacked column-wise for each transmitted sub-vector. Notice that this can be done because the rows of $(\mathbf{u}_{M, K, \tilde{\nu}})^T$ are the same for a particular column. Then, the element-wise division by the data leads to $(\mathbf{F}_K \mathbf{Y}_{\text{ofdm}}) \circledast \mathbf{D} \approx (\mathbf{u}_{M, K, \tilde{\nu}})^T \circledast \mathbf{G}_{K, M, \tilde{\tau}}$, removing the data symbol. After that, the IDFT $\mathbf{F}_K^H ((\mathbf{F}_K \mathbf{Y}_{\text{ofdm}}) \circledast \mathbf{D}) \approx (\mathbf{u}_{M, K, \tilde{\nu}})^T \circledast \mathbf{g}_{K, M, \tilde{\tau}}$ recovers back the raise cosine filter in time domain. Since the Doppler shift is encoded in the linear phase shift of $\mathbf{u}_{M, \tilde{\nu}}$, the phase shift can be estimated by the IDFT of size M , which is achieved by transposing the previous result and taking the IDFT as $\mathbf{F}_M^H (\mathbf{F}_K^H ((\mathbf{F}_K \mathbf{Y}_{\text{ofdm}}) \circledast \mathbf{D}))^T \approx \mathbf{F}_M^H (\mathbf{u}_{M, K, \tilde{\nu}})^T \circledast (\mathbf{g}_{K, M, \tilde{\tau}})^T = (\mathbf{v}_{M, K, \tilde{\nu}}) \circledast (\mathbf{g}_{K, M, \tilde{\tau}})^T = \mathbf{v}_{M, \tilde{\nu}} \mathbf{g}_{K, \tilde{\tau}}^T$ has size $M \times K$, where $\mathbf{v}_{M, K, \tilde{\nu}} = \mathbf{F}_M^H \mathbf{u}_{M, K, \tilde{\nu}}$ and $\mathbf{v}_{M, \tilde{\nu}} = \mathbf{F}_M^H \mathbf{u}_{M, \tilde{\nu}}$.

The multiple target extension follows directly from (63) since the model is additive.

C. Bistatic Radar Geometry

Let $P_{\text{bs}} = (x_{\text{bs}}, y_{\text{bs}})$, $P_{\text{t}} = (x_{\text{t}}, y_{\text{t}})$ and $P_{\text{r}} = (x_{\text{r}}, y_{\text{r}})$ be the coordinates of the BS, target and radar, respectively, in the $x \times y$ plane. The distances BS-target, target-radar and BS-radar are given doted by d_{BT} , d_{TR} and d_{BR} , respectively. Without loss of generality, we place the BS and radar at $P_{\text{bs}} = (-d_{\text{BR}}/2, 0)$ and $P_{\text{r}} = (d_{\text{BR}}/2, 0)$.

1) *Maximum Delay Iso-range Contour*: Taking the LoS path as a reference, the target delay is given by $\tau = (d_{\text{BT}} + d_{\text{TR}} - d_{\text{BR}})/c$, we c is the speed of light. The maximum unambiguous delay τ^{max} of the Subsection VI-C determines the maximum distance $d_{\text{max}} = \tau^{\text{max}} c + d_{\text{BR}} \geq d_{\text{BT}} + d_{\text{TR}}$

that the signal from the BS to the radar can travel, such that the $\tau \leq \tau^{\max}$. The iso-range contour is defined by an ellipse that describes the target's coordinates that satisfy $d_{\max} = d_{\text{BT}} + d_{\text{TR}}$, whose coordinates are

$$\begin{aligned} x_t &= \frac{d_{\max}}{2} \cos(t) \\ y_t &= 1/2 \sqrt{(\tau^{\max}c)^2 + 2d_{\text{BR}}\tau^{\max}c} \sin(t) \quad \text{for } 0 \leq t < 2\pi \end{aligned} \quad (64)$$

for $0 \leq t < 2\pi$.

2) *Waterfall SNR Cassini Oval*: For a constant $b > 0$, the Cassini oval defines a set of coordinates of \mathcal{P}_t which satisfies $d_{\text{BT}}d_{\text{TR}} = b^2$. In the bistatic radar scenario, the Cassini oval is useful to determine the coordinates $P_t = (x_t, y_t)$ which attain a given desired SNR ρ^* for the channel model of (59). In this case, the constant b^2 is

$$b^2 = d_{\text{BT}}d_{\text{TR}} = \left(\frac{P_{\text{bs}}GG_{\text{bs}}G_{\text{r}}\lambda^2\sigma_{\text{rCS}}}{\rho^*\tilde{\sigma}_{\text{w}}^2(4\pi)^3} \right)^{\frac{1}{\eta}}. \quad (65)$$

From [34], the coordinates P_t satisfying (65) are

$$x_t = \frac{b^4 - t^4}{4d_{\text{BR}}t^2} \quad \text{and} \quad y_t = \pm \sqrt{t^2 - (x - d_{\text{BR}})^2}, \quad (66)$$

for $d_{\text{BR}} + \sqrt{d_{\text{BR}}^2 - b^2} \leq t \leq d_{\text{BR}} + \sqrt{d_{\text{BR}}^2 + b^2}$ if $d_{\text{BR}} \geq b$, and $-d_{\text{BR}} + \sqrt{d_{\text{BR}}^2 + b^2} \leq t \leq d_{\text{BR}} + \sqrt{d_{\text{BR}}^2 + b^2}$ otherwise.

REFERENCES

- [1] M. Chafii, L. Bariah, S. Muhaidat, and M. Debbah, "Twelve scientific challenges for 6G: Rethinking the foundations of communications theory," *IEEE Commun. Surv. Tutor.*, vol. 25, no. 2, pp. 868–904, 2023.
- [2] F. Liu *et al.*, "Integrated sensing and communications: Toward dual-functional wireless networks for 6g and beyond," *IEEE J. Sel. Areas Commun.*, vol. 40, no. 6, pp. 1728–1767, 2022.
- [3] J. A. Zhang, M. L. Rahman, K. Wu, X. Huang, Y. J. Guo, S. Chen, and J. Yuan, "Enabling joint communication and radar sensing in mobile networks—a survey," *IEEE Commun. Surv. Tutor.*, vol. 24, no. 1, pp. 306–345, 2022.
- [4] T. M. Pham, R. Bomfin, A. Nimr, A. N. Barreto, P. Sen, and G. Fettweis, "Joint communications and sensing experiments using mmwave platforms," in *2021 IEEE 22nd International Workshop on Signal Processing Advances in Wireless Communications (SPAWC)*, pp. 501–505, 2021.
- [5] D. Ma, N. Shlezinger, T. Huang, Y. Liu, and Y. C. Eldar, "Joint radar-communication strategies for autonomous vehicles: Combining two key automotive technologies," *IEEE Signal Processing Mag.*, vol. 37, no. 4, pp. 85–97, 2020.
- [6] J. A. Zhang *et al.*, "An overview of signal processing techniques for joint communication and radar sensing," *IEEE Journal of Selected Topics in Signal Processing*, vol. 15, no. 6, pp. 1295–1315, 2021.
- [7] C. Sturm and W. Wiesbeck, "Waveform design and signal processing aspects for fusion of wireless communications and radar sensing," *Proc. IEEE*, vol. 99, no. 7, pp. 1236–1259, 2011.
- [8] C. Baquero Barneto *et al.*, "Full-duplex OFDM radar with LTE and 5G NR waveforms: Challenges, solutions, and measurements," *IEEE Trans. Microw. Theory. Tech.*, vol. 67, no. 10, pp. 4042–4054, 2019.
- [9] J. Johnston, L. Venturino, E. Grossi, M. Lops, and X. Wang, "MIMO OFDM dual-function radar-communication under error rate and beam-pattern constraints," *IEEE J. Sel. Areas Commun.*, vol. 40, no. 6, pp. 1951–1964, 2022.
- [10] S. H. Dokhanchi, A. N. Barreto, and G. P. Fettweis, "Performance analysis of zero-padded sequences for joint communications and sensing," *IEEE Trans. Signal Process.*, vol. 71, pp. 1725–1741, 2023.
- [11] F. Liu, L. Zhou, C. Masouros, A. Li, W. Luo, and A. Petropulu, "Toward dual-functional radar-communication systems: Optimal waveform design," *IEEE Trans. Signal Process.*, vol. 66, no. 16, pp. 4264–4279, 2018.
- [12] A. Bazzi and M. Chafii, "On outage-based beamforming design for dual-functional radar-communication 6G systems," *IEEE Trans. Wireless Commun.*, vol. 22, no. 8, pp. 5598–5612, 2023.
- [13] A. Bazzi and M. Chafii, "On integrated sensing and communication waveforms with tunable PAPR," *IEEE Trans. Wireless Commun.*, vol. 22, no. 11, pp. 7345–7360, 2023.
- [14] A. Chowdhury, A. Bazzi, and M. Chafii, "On hybrid radar fusion for integrated sensing and communication," *IEEE Trans. Wireless Commun.*, pp. 1–1, 2024.
- [15] L. Gaudio, M. Kobayashi, G. Caire, and G. Colavolpe, "On the effectiveness of ofds for joint radar parameter estimation and communication," *IEEE Trans. Wireless Commun.*, vol. 19, no. 9, pp. 5951–5965, 2020.
- [16] M. F. Keskin, H. Wymeersch, and A. Alvarado, "Radar sensing with OTFS: Embracing ISI and ICI to surpass the ambiguity barrier," in *2021 IEEE International Conference on Communications Workshops (ICC Workshops)*, pp. 1–6, 2021.
- [17] Z. Gong, F. Jiang, C. Li, and X. Shen, "Simultaneous localization and communications with massive mimo-ofds," *IEEE J. Sel. Areas Commun.*, vol. 41, no. 12, pp. 3908–3924, 2023.
- [18] P. Kumari, J. Choi, N. González-Prelcic, and R. W. Heath, "IEEE 802.11ad-based radar: An approach to joint vehicular communication-radar system," *IEEE Trans. Veh. Technol.*, vol. 67, no. 4, pp. 3012–3027, 2018.
- [19] J. Pegoraro *et al.*, "JUMP: Joint communication and sensing with unsynchronized transceivers made practical," *IEEE Trans. Wireless Commun.*, pp. 1–1, 2024.
- [20] Z. Wei and al, "5G PRS-based sensing: A sensing reference signal approach for joint sensing and communication system," *IEEE Trans. Veh. Technol.*, vol. 72, no. 3, pp. 3250–3263, 2023.
- [21] L. Deneire, B. Gyselinckx, and M. Engels, "Training sequence versus cyclic prefix—a new look on single carrier communication," *IEEE Commun. Lett.*, vol. 5, no. 7, pp. 292–294, 2001.
- [22] J. Coon, M. Sandell, M. Beach, and J. McGeehan, "Channel and noise variance estimation and tracking algorithms for unique-word based single-carrier systems," *IEEE Trans. Wireless Commun.*, vol. 5, no. 6, pp. 1488–1496, 2006.
- [23] M. Huemer, H. Witschnig, and J. Hausner, "Unique word based phase tracking algorithms for SC/FDE-systems," in *GLOBECOM '03. IEEE Global Telecommunications Conference*, vol. 1, pp. 70–74 Vol.1, 2003.
- [24] S. Ehsanfar, M. Chafii, and G. P. Fettweis, "On UW-based transmission for MIMO multi-carriers with spatial multiplexing," *IEEE Trans. Wireless Commun.*, vol. 19, no. 9, pp. 5875–5890, 2020.
- [25] R. Bomfin, M. Chafii, A. Nimr, and G. Fettweis, "A robust baseband transceiver design for doubly-dispersive channels," *IEEE Trans. Wireless Commun.*, vol. 20, no. 8, pp. 4781–4796, 2021.
- [26] R. Bomfin, M. Chafii, and G. Fettweis, "A novel iterative receiver design for CP-free transmission under frequency-selective channels," *IEEE Commun. Lett.*, vol. 24, no. 3, pp. 525–529, 2020.
- [27] R. Bomfin and M. Chafii, "Unique word-based frame design for bistatic ISAC with time-domain filtering," in *2024 IEEE Global Communications Conference (GLOBECOM)*, p. 5.93, Dec. 2024.
- [28] K. Wu *et al.*, "Sensing in bi-static ISAC systems with clock asynchronism: A signal processing perspective," *arXiv preprint*, 2024. arXiv:2402.09048.
- [29] N. B. Khoolejani and K. Khorshidian, "On the ratio of rice random variables," *Journal of the Iranian Statistical Society*, vol. 8, pp. 61–71, 2009.
- [30] E. Díaz-Francés and F. J. Rubio, "On the existence of a normal approximation to the distribution of the ratio of two independent normal random variables," *Statistical Papers*, vol. 54, pp. 309–323, 2013.
- [31] G. Casella and R. L. Berger, *Statistical Inference*. USA: Duxbury, 2002.
- [32] Y. Xing and T. S. Rappaport, "Millimeter wave and terahertz urban microcell propagation measurements and models," *IEEE Commun. Lett.*, vol. 25, no. 12, pp. 3755–3759, 2021.
- [33] T. S. Rappaport *et al.*, "Millimeter wave mobile communications for 5g cellular: It will work!," *IEEE Access*, vol. 1, pp. 335–349, 2013.
- [34] R. Ferréol, "Cassini Oval," 2017. [Online]. Available: <https://mathcurve.com/courbes2d.gb/cassini/cassini.shtml>.